The Astrophysical Journal, 892:37 (17pp), 2020 March 20 https://doi.org/10.3847/1538-4357/ab77ab

Properties of Trans-fast Magnetosonic Jets in Black Hole Magnetospheres

Hung-Yi Pu[1] and Masaaki Takahashi[2]
[1] Perimeter Institute for Theoretical Physics, 31 Caroline Street North, Waterloo, ON, N2L 2Y5, Canada
[2] Department of Physics and Astronomy, Aichi University of Education, Kariya, Aichi 448-8542, Japan
Received 2019 June 8; revised 2020 February 3; accepted 2020 February 17; published 2020 March 24

Abstract

Traveling across several orders of magnitude in distance, relativistic jets from strong gravity regions to asymptotic flat spacetime regions are believed to consist of several general relativistic magnetohydrodynamic (GRMHD) processes. We present a semianalytical approach for modeling the global structures of a trans-fast magnetosonic relativistic jet, which should be ejected from a plasma source near a black hole in a funnel region enclosed by dense accreting flow and a disk corona around the black hole. Our model consistently includes the inflow and outflow part of the GRMHD solution along the magnetic field lines penetrating the black hole horizon. After the rotational energy of the black hole is extracted electromagnetically by the negative energy GRMHD inflow, the huge electromagnetic energy flux propagates from the inflow to the outflow region across the plasma source, and in the outflow region, the electromagnetic energy converts to the fluid kinetic energy. Eventually, the accelerated outflow must exceed the fast magnetosonic wave speed. We apply the semianalytical trans-fast magnetosonic flow model to the black hole magnetosphere for both parabolic and split-monopole magnetic field configurations and discuss the general flow properties, that is, jet acceleration, jet magnetization, and the locations of some characteristic surfaces of the black hole magnetosphere. We have confirmed that, at large distances, the GRMHD jet solutions are in good agreement with the previously known trans-fast special relativistic magnetohydrodynamic jet properties, as expected. The flexibility of the model provides a prompt and heuristic way to approximate the global GRMHD trans-fast magnetosonic jet properties.

Unified Astronomy Thesaurus concepts: Rotating black holes (1406); Relativistic jets (1390); Magnetic fields (994); Magnetohydrodynamics (1964); Galaxy jets (601); Jets (870); Black hole physics (159); Astrophysical black holes (98); Kerr black holes (886); Accretion (14)

1. Introduction

Black holes with accreting matter are believed to be the central engines of the observed relativistic jets from microquasars (Fender et al. 2004; Miller-Jones et al. 2012; Rushton et al. 2017), active galactic nuclei (AGNs; Homan et al. 2015; Hada et al. 2016; Bruni et al. 2017; Pushkarev et al. 2017; McKinley et al. 2018), and presumably gamma-ray bursts (Chang et al. 2012; Nava et al. 2017; Ryde et al. 2017). Traveling across several orders of magnitude in distance from the black hole horizon ($r \sim r_{\rm g}$, where $r_{\rm g} = GM_{\bullet}/c^2$ is the gravitational radius and $M_{\bullet}$ is the black hole mass) to large distances, a relativistic jet formulated in the magnetosphere of a black hole is among the most efficient ways to accelerate particles and redistribute energy and angular momentum from small to large scales. For example, jets from AGNs can extend to a scale larger than the Bondi radius ($\sim 10^{5-6} r_{\rm g}$; e.g., Algaba et al. 2017) and even larger than the size of the host galaxy ($>10^{8-9} r_{\rm g}$), providing mechanical feedback to the galaxy clusters (e.g., Fabian 2012).

Supported by much observational evidence (e.g., Hovatta et al. 2012; Kino et al. 2014; Asada et al. 2014), it is believed that a large-scale magnetic field plays an important role in extracting the energy from the central region and accelerating and collimating the jet. The current understanding of the relativistic jets in the magnetohydrodynamical framework, including both the special relativistic magnetohydrodynamics (SRMHD; excluding the effect of gravity) and the general relativistic magnetohydrodynamics (GRMHD; including the effect of gravity), provides the following picture. At the footpoint region of the jet, where the strong gravity of the central black hole must be considered, a large-scale magnetic field penetrates the black hole horizon at least near the funnel region of accreting gas, and the rotational energy of the black hole would be electromagnetically extracted outward by the GRMHD flow (e.g., Blandford & Znajek 1977; Takahashi et al. 1990; Koide 2003; Hawley & Krolik 2006; McKinney 2006). At a far region from the central black hole, where spacetime becomes almost flat and SRMHD becomes a good approximation, the magnetic energy gradually converts to particle kinetic energy, and the flow accelerates to its terminal velocity (Camenzind 1986a, 1986b, 1987; Fendt et al. 1995; Fendt & Camenzind 1996; Beskin et al. 1998; Takahashi & Shibata 1998; Fendt & Greiner 2001; Vlahakis 2004; Beskin & Nokhrina 2006; Tchekhovskoy et al. 2008, 2009, 2010; Komissarov et al. 2009; Lyubarsky 2009, 2010).

More specifically, a full and consistent model of black hole jet formation across several orders of magnitude in distance, from the near zone ($r \sim r_g$) to the far zone ($r > 10^{4-5} r_g$), is challenging due to at least the following three reasons. The first is the configuration of the magnetic fields. The equation of motion for the MHD flow,

$$T^{\mu\nu}_{;\nu} = 0, \tag{1}$$

where the stress energy tensor $T^{\mu\nu} = T^{\mu\nu}_{\rm EM} + T^{\mu\nu}_{\rm FL}$ consists of the electromagnetic part $T^{\mu\nu}_{\rm EM}$ and the fluid part $T^{\mu\nu}_{\rm FL}$, can be decomposed into the *force-balance equation* between magnetic field lines (the Grad–Shafranov equation) and the *wind equation* along a magnetic field line (the relativistic Bernoulli equation). The former describes the magnetic field configuration, while the latter describes the jet acceleration

(Nitta et al. 1991; Beskin 2009). However, in general, solving the force-balance equation analytically is complicated and usually computationally demanding (e.g., Fendt et al. 1995; Fendt & Camenzind 1996; Nathanail & Contopoulos 2014; Pan et al. 2017; Huang et al. 2019). The second reason is the condition at the fast magnetosonic surface (FMS) of the jet, where the jet velocity becomes the fast magnetosonic wave speed. The FMS should be located at a finite radius on the way to a distant region in the black hole magnetosphere (Fendt 1997; Beskin et al. 1998; Tomimatsu et al. 2001; Beskin & Nokhrina 2006). Generally, a complicated critical-condition analysis at the FMS is required. The third reason is related to the plasma source region of the jet. In the black hole magnetosphere, due to the dominant gravity near the black hole and the dominant centrifugal force by the Lorentz force away from the black hole, the inflow and outflow regions, and therefore a stagnation surface, must coexist (Takahashi et al. 1990; McKinney & Gammie 2004; McKinney 2006), where the stagnation surface separates the inflow/outflow regions. At the stagnation surface, a matching condition for the two zones is necessary (Pu et al. 2015), where additional discussion of the state of the plasma source should be required (e.g., the electron-position pair creation, etc.). With these difficulties, to date, exploring GRMHD jet properties in both near and far regions was mostly possible by performing a large-scale GRMHD simulation (e.g., McKinney 2006; Liska et al. 2018; Chatterjee et al. 2019). Furthermore, in the funnel region close to the black hole axis that we are interested in here, the radially self-similar approach (Blandford & Payne 1982; Vlahakis et al. 2000; Polko et al. 2013, 2014) is not applicable, while the meridional self-similarity can provide a more suitable alternative (Sauty & Tsinganos 1994; Meliani et al. 2006; Tsinganos 2010; Globus et al. 2014; Chantry et al. 2018).

In this paper, we present a semianalytical approach, an attractive alternative, to include the key features of the abovementioned physical processes. We especially focus on magnetic energy-dominated flows that are capable of extracting the black hole rotational energy near the plasma source and kinetic energy-dominated jet structure at a far distant region. The presented model provides a prompt, flexible, and heuristic way to investigate the trans-fast magnetosonic jet structures and properties semianalytically. Our model is an application of solving the relativistic Bernoulli equation along magnetic field lines in an algebraic way via prescriptions of the poloidal and toroidal (azimuthal) magnetic fields (Tomimatsu & Takahashi 2003; Takahashi & Tomimatsu 2008, hereafter TT03 and TT08, respectively) and of consistently matching the inflow/outflow flow solutions (Pu et al. 2015). In contrast to the standard approaches for transmagnetosonic flow, which employ the regularity condition on the FMS to solve the relativistic Bernoulli equation (e.g., Takahashi et al. 1990; Takahashi 2002), the novel approach provided by the former works, TT03 and TT08, is to solve the jet's Bernoulli equation by introducing a regular function of the poloidal electric-to-toroidal magnetic field amplitude ratio, ξ, in all regions of the jet. This allows us to obtain easily trans-fast magnetosonic flow solutions for relativistic jets without the regularity condition analysis. The function ξ has sophisticated constraints on the magnetic field components at several characteristic surfaces, such as the particle injection surface, Alfvén surface, event horizon, etc. (see also Section 2.2). The idea that the outflow along the magnetic field lines in a magnetosphere can be determined by the distribution of poloidal and toroidal fields has also been discussed in Contopoulos (1995) and Contopoulos et al. (1999).

The purpose of this paper is to demonstrate that the basic GRMHD jet structure can actually be well approximated from the abovementioned approaches. The underlying physical motivation is to mimic the GRMHD flow solution of Equation (1) with the knowledge of GRMHD theory, including some solutions of the force-balance equation and how the magnetosonic points are related to the solution of wind equations (see Section 2). We ignore the gas pressure in the flow, which is minor for the global flow structure (Camenzind 1986b), and adopt the cold limit in our computations. Under such a limit, the stagnation surface can be solely determined by the locus across field lines where the force balance between gravity force and magnetocentrifugal force, provided that the flow has vanishing initial velocity (or very slow sub-Alfvénic velocity). As the plasma loading is conserved along each field line (see Section 2), the stagnation surface is treated as the plasma source region. The plasma source in the jet funnel region, which is beyond the scope of the current paper, is currently poorly understood (e.g., Takahashi et al. 1990; Levinson & Rieger 2011; Mościbrodzka et al. 2011; Broderick & Tchekhovskoy 2015; Hirotani & Pu 2016; O'Riordan et al. 2018). Nevertheless, comparison of the flow velocity and magnetic field configuration between the numerical simulation[3] and the semianalytical solution along a large-scale magnetic field line in the funnel region shows similar properties (Pu et al. 2015), indicating that the GRMHD flow velocity is not significantly affected by the plasma source.

We do not solve the force-balance equation for the configuration of the magnetic field but instead assume a likely magnetic field shape. We are especially interested in the parabolic and split-monopole poloidal magnetic fields, because there are extensive SRMHD studies for the trans-fast magnetosonic flow in these two magnetic configurations (e.g., Beskin et al. 1998; TT03; Beskin & Nokhrina 2006), and we can compare our GRMHD flow solutions with the SRMHD flow features. Note also that a parabolic magnetic field geometry is commonly indicated by very long baseline interferometry observations of AGN jets (e.g., Algaba et al. 2017; Hada et al. 2013; Nakamura et al. 2018), and it is a common scene of GRMHD numerical simulations of an accreting black hole system (e.g., McKinney & Gammie 2004; Hawley & Krolik 2006; McKinney 2006). Therefore, we choose to apply our model to these magnetic fields and explore the general flow properties near the black hole, the jet acceleration of the outflow, and the characteristic surfaces, together with their dependence on black hole spin, field angular velocity, and outflow energy. In the region far away from the black hole, the resulting semianalytical GRMHD outflow acceleration is in good qualitative and quantitative agreement with previous analyses of semianalytical MHD flow acceleration properties (TT03; Beskin et al. 1998; Beskin & Nokhrina 2006).

The remainder of the paper is organized as follows. In Section 2 we describe the details of the model. The model

[3] In numerical simulation, to avoid numerical issues, a density floor is usually set to ensure a minimum density in the simulation; materials are therefore arbitrarily injected into the funnel region, which usually takes place close to the central black hole.

parameters considered in this paper are given in Section 3. We then present the results and GRMHD flow properties in a black hole magnetosphere with parabolic and split-monopole magnetic field lines in Sections 4 and 5, respectively. Comments on the limitations of the model are given in Section 6. Finally, the summary and future applications of the model are given in Section 7.

2. Trans-fast Magnetosonic Flows in a Black Hole Magnetosphere

Our goal is develop a semianalytical approach to model a trans-fast magnetosonic flow with a very large total specific energy along magnetic field lines attached to the horizon and include all related key physics. While it is well known that mild plasma loading can result in a slight deformation of the magnetic field lines and the existence of the FMS by carefully solving both the trans-field and wind equations, the following working compromise is adopted. First, a poloidal force-free magnetic field configuration is applied (i.e., the deformation of the magnetic fields due to the perturbation via plasma loading is ignored). Second, to preserve the existence of the FMS for an MHD flow, a sophisticated relation between the poloidal and toroidal components of the magnetic field is prescribed a priori (TT08).

As the model is an extension of the method presented in TT08, in the following, we adopt the same signature [+, −, −, −] for the Boyer–Lindquist metric, with $c = G = 1$. The dimensionless black hole spin parameter is denoted by a.

2.1. Basic GRMHD Flow Properties

We assume a cold ideal GRMHD flow where the gas pressure is negligible. Then, there are four conserved quantities along the magnetic field line given by the magnetic stream function $\Psi(r, \theta) =$ constant (Camenzind 1986a, 1986b, 1987; Takahashi et al. 1990): the angular velocity of the field line $\Omega_F(\Psi)$, the particle number flux per unit electromagnetic flux (mass loading) $\eta(\Psi)$, the total energy of the flow $E(\Psi)$, and the total angular momentum $L(\Psi)$,

$$\Omega_F(\Psi) = -\frac{F_{t\theta}}{F_{\theta\phi}}, \tag{2}$$

$$\mu\eta(\Psi) = \frac{n\mu u_p}{\bar{B}_p}, \tag{3}$$

$$\hat{E}(\Psi) \equiv \frac{E(\Psi)}{\mu} = u_t - \frac{\Omega_{\rm F} B_\phi}{4\pi\mu\eta}, \tag{4}$$

$$\hat{L}(\Psi) \equiv \frac{L(\Psi)}{\mu} = -u_\phi - \frac{B_\phi}{4\pi\mu\eta}, \tag{5}$$

where $F_{\mu\nu}$ is the electromagnetic tensor, the magnetic field $B_\alpha \equiv (1/2)\epsilon_{\alpha\beta\gamma\delta}k^\beta F^{\gamma\delta}$ is defined by the time-like Killing vector $k^\alpha = (1, 0, 0, 0)$, and $\epsilon_{\alpha\beta\gamma\delta}$ is the Levi–Civita tensor. The hat symbols for $\hat{E}$ and $\hat{L}$ represent the physical quantities per specific enthalpy, μ, which is given by $\mu = m_{\rm p}c^2$ (the speed of light c is momentarily recovered here), where $m_{\rm p}$ is the particle's rest mass. In addition, the poloidal velocity and magnetic field are respectively defined by $u_p^2 \equiv -(u^r u_r + u^\theta u_\theta)$ and $B_p^2 \equiv -(B^r B_r + B^\theta B_\theta)$, and the rescaled poloidal magnetic field is defined by

$$\bar{B}_p^2 \equiv B_p^2/\rho_w^2, \tag{6}$$

where $\rho_w^2 = g_{t\phi}^2 - g_{tt}g_{\phi\phi}$. Similarly, we define the rescaled toroidal magnetic field by

$$\bar{B}_\phi \equiv B_\phi/\rho_w. \tag{7}$$

Along the large-scale magnetic field immersed in the black hole, there must exist inflow and outflow regions, divided by the location of the stagnation surface $r_s(\Psi)$. In the cold limit, the conservative quantities $(\hat{E}, \hat{L})$ can be alternatively determined by $(r_{\rm s}, r_{\rm A})$, where $r_{\rm A} = r_{\rm A}(\Psi)$ is the location of the Alfvén surface, where the flow velocity equals the poloidal Alfvén speed (Takahashi et al. 1990). Hereafter, we denote the inflow (or outflow) properties by the superscript "−" (or "+") and use the unsigned parameters for the base for both inflow and outflow. We focus on cases where black hole rotational energy is extracted outward as the energy budget of the GRMHD flow, and the model applies for all rotating black holes ($a > 0$), with $0 < \Omega_F < \Omega_{\rm H}$ (i.e., the "type II" flow defined in Takahashi et al. 1990), where $\Omega_{\rm H}$ is the angular velocity of the black hole.

2.2. Overview of TT08

For a given streamline function and therefore the poloidal magnetic field configuration, a typical procedure for solving the wind equation along a streamline function then requires fine-tuning of the set of conserved quantities, Ω_F, η, $\hat{E}$, $\hat{L}$, such that a physical cold flow solution passes both the Alfvén surface and the FMS, where the so-called critical condition should be satisfied. When the physical flow solution is obtained, the toroidal magnetic field structure is uniquely determined that should be regular in all regions of the flow. Note that, without the critical condition at the FMS, the toroidal magnetic field diverges there; i.e., such a solution is unphysical.

To always get a physical trans-fast magnetosonic solution, we focus on the regularity of the toroidal magnetic field. Now we introduce a regular function by relating the ratio between the poloidal and toroidal magnetic field to the parameter β,

$$\beta(r; \Psi) \equiv \frac{B_\phi}{B_p} = \frac{\bar{B}_\phi}{\bar{B}_p}. \tag{8}$$

A regular transmagnetosonic flow solution can therefore be obtained; such a new analytical method without the critical conditions is proposed in TT08. The parameter β can be interpreted as the inverse of the pitch angle or the bending angle of the magnetic field line. Alternatively, related to β, the poloidal electric-to-toroidal magnetic field amplitude ratio seen by a zero angular momentum observer can be defined by

$$\xi^2(r; \Psi) = g_{\phi\phi}\frac{(\Omega_F - \omega)^2}{\beta^2}, \tag{9}$$

where $\omega \equiv -g_{t\phi}/g_{\phi\phi}$.

As a result, by defining the Alfvén Mach number,

$$M^2 = 4\pi\mu n\frac{u_p^2}{\bar{B}_p^2} = 4\pi\mu\eta\frac{u_p}{\bar{B}_p^2}, \tag{10}$$

the wind equation can be rewritten with the quadratic equation

$$\mathcal{A}M^4 - 2\mathcal{B}M^2 + \mathcal{C} = 0, \tag{11}$$

where the coefficients $\mathcal{A}$, $\mathcal{B}$, and $\mathcal{C}$ are just functions of the conserved quantities Ω_F, $\hat{E}$, and $\hat{L}$; the magnetic field pitch angle, β; and the background metric, $g_{\mu\nu}$. Readers can refer

Table 1
Restrictions on the Regular Function ξ at Several Characteristic Locations for a Physical Solution of the Wind Equation that Passes an FMS

Characteristic Location	ξ^2
Event horizon	1
Corotation point[a]	0
Alfvén point	Finite
Separation point	Finite

Note.
[a] Where $\Omega_F = \omega$.

to TT08 for details. The location of the Alfvén surface and FMS[4] of the flow can be found where the Mach number equals

$$M^2 = M_{\rm AW}^2 \equiv \alpha, \tag{12}$$

$$M^2 = M_{\rm FM}^2 \equiv \alpha + \beta^2, \tag{13}$$

where $\alpha = g_{tt} + 2g_{t\phi}\Omega_F + g_{\phi\phi}\Omega_F^2$. The poloidal velocity is

$$u_p^2 = \frac{\hat{e}^2 - \alpha}{\alpha + \beta^2}, \tag{14}$$

with the Jacobian constant $\hat{e} \equiv \hat{E} - \Omega_F \hat{L}$.

By solving the wind equation in terms of β (or, alternatively, ξ), the restriction for β and ξ when FMS exists in the solution is found. For our interest, $0 < \Omega_F < \Omega_{\rm H}$, the conditions are summarized in Table 1 (see also Appendix A of TT08). Along a magnetic field line Ψ = constant, the function $\xi^2(r; \Psi)$ would have a different form in the inner and outer region of the separation surface (the plasma source). For the outflow, by considering the reasonable shape of the magnetic field at a distant region, we apply the function form

$$(\xi^+)^2 = 1 - \frac{1}{(\hat{E}^+)^2} + \zeta_0, \tag{15}$$

where ζ_0 is a constant associated with the flow acceleration in the superfast-magnetosonic regime. Previous extensive studies of the SRMHD flow acceleration indicate a dependence on different magnetic field geometry (e.g., Beskin et al. 1998; Beskin & Nokhrina 2006; Tchekhovskoy et al. 2008, 2009; Komissarov et al. 2009). We explored different choices of ζ_0 and identified that $\zeta_0 \cong 0$ corresponds to a *linear acceleration* regime of the flow (in contrast to a slower, *logarithmic acceleration*; see more details in Appendix B). We therefore adopt

$$\zeta_0 = 0 \tag{16}$$

as the default value throughout the paper. Although we consider a constant $(\xi^+)^2$ along a flow, it is not generally necessary. Note that a constant $(\xi^+)^2$ along a magnetic field line recovers that the ratio of the poloidal to toroidal field is well fit by $1/(\Omega_F\sqrt{g_{\phi\phi}})$ (see also Section 4.1 for examples), as expected in the SRMHD jet studies (e.g., Lyubarsky 2009) and also found in previous GRMHD simulations (McKinney 2006).

For the inflow from both the requirement at the horizon and the corotation point listed in Table 1, a sophisticated form of ξ was suggested in TT08,

$$(\xi^-)^2 = \left[1 + C\frac{\Delta}{\Sigma}\right]\left(\frac{\omega - \Omega_F}{\Omega_{\rm H} - \Omega_F}\right)^2, \tag{17}$$

where C is a constant. For our interest, C is to be determined by a smooth connect for ξ^+ and ξ^- (see also Section 2.5 for the matching condition for outflow and inflow). Unlike $(\xi^+)^2$, $(\xi^-)^2$ cannot be a constant along the magnetic field line, as can also be seen in Table 1.

2.3. Magnetic Field Configurations

We focus on magnetically dominated flow, at least in the jet formation region, and therefore assume the force-free magnetosphere is a good approximation for the magnetic field configuration.[5] A simple approximation of the force-free magnetic field is found in Tchekhovskoy et al. (2008),

$$\Psi(r, \theta; p) = r^p(1 - \cos\theta), \tag{18}$$

where $0 \leqslant p \leqslant 1.25$. When $p = 1$ ($p = 0$), the magnetic field has a parabolic (split-monopole) configuration. In general, the magnetosphere depends on parameters like black hole spin. Recent GRMHD numerical simulations imply that a single p value for the outmost streamline may apply to simulation results of different black hole spin (Nakamura et al. 2018), and that the resulting opening angle of the magnetosphere is closely related the total magnetic flux finally accumulated on the event horizon (e.g., Narayan et al. 2012), suggesting treating the black hole spin and magnetosphere as independent parameters for possible combinations.

One of the features of the abovementioned force-free magnetic field is the absence of the FMS of the outflow. The resulting magnetic flux $\Phi \equiv \bar{B}_{\rm p} R^2$ of Equation (18) is roughly constant at large distances, which is against the condition $d\Phi/dR < 0$ for an efficient MHD acceleration and the existence of FMS (Takahashi & Shibata 1998; Tchekhovskoy et al. 2009). As a result, the outflow along the force-free magnetic field will remain sub-fast magnetosonic if we simply solve the Bernoulli equation and obtain the toroidal field from the solution. We therefore overcome the nonexistence of an FMS for the poloidal magnetic field described in Equation (18) by prescribing a relation between the poloidal and toroidal magnetic fields of the resulting flow, a method introduced in TT03 and TT08, to mimic the effect of efficient acceleration for the outflow. By using this method, the solution for the trans-fast magnetosonic flow equation can be easily obtained without the critical-condition analysis. However, as a cost for this approach, it is expected that $\bar{B}_p$ computed directly from Equation (18) would not be consistent with the solution of the force-balance equation due to the reason mentioned before. We will therefore obtain $\bar{B}_p$ from the trans-fast magnetosonic flow solution, as will be described in Section 2.7.

[4] It is expected that, close to the axis ($\theta \to 0$), $\beta \to 0$ and hence $M_{\rm FM}^2 = M_{\rm AW}^2$, resulting a closer distance between the Alfvén surface and FMS (see also Beskin et al. 1998; Beskin 2009; Tchekhovskoy et al. 2009). Such an effect is caused by the modification of the force-free magnetosphere due to plasma effects, and our approach can at most provide only an artificial mimic to such an effect, since the poloidal magnetic field configuration is prescribed and fixed in the computation, as explained and described in Section 2.3.

[5] Nevertheless, the semianalytical method described in this section can be applied to any given physical magnetic configuration Ψ.

2.4. Boundary Condition

The energy of the outflow $\hat{E}^+$ is assigned for each magnetic field line as the outer boundary. Across the black hole magnetosphere, $\hat{E}^+(\Psi)$ is a free function, which is not necessary a constant across the magnetosphere. For each streamline with known Ω_F, specified flow energy $\hat{E}^+$, and location of flow launching with zero velocity r_s, the location of the Alfvén surface, r_A^+, can be solved by Equation (11). Subsequently, the angular momentum for the outflow $\hat{L}^+$ are also determined[6] (e.g., see Equations (43) and (44) of Takahashi et al. 1990; see also Appendix A for a flowchart).

2.5. Matching Condition

Two criteria are required to be satisfied in order to match the inflow and outflow solutions along each magnetic field line.

First, to ensure that $B^2 = B_p^2 + B_\phi^2$ is continuous across the stagnation surface r_s, the constant C is determined by

$$\xi^-(r_s; \Psi) = \xi^+(r_s; \Psi). \tag{19}$$

Second, in addition to the continuity of the magnetic field strength, it is also expected that the outward electromagnetic energy flux is continuous across r_s. However, such a condition is degenerate and leaves an undetermined ratio (Pu et al. 2015),

$$\delta = \left| \frac{\hat{E}^+_{\rm EM}}{\hat{E}^-_{\rm EM}} \right| = \left| \frac{\eta^-}{\eta_+} \right|; \tag{20}$$

note that $\hat{E}^+_{\rm EM} > 0$ and $\hat{E}^-_{\rm EM} < 0$ (i.e., negative energy GRMHD inflows) have different signs. The nature of the degeneracy of the choice of δ lies in the fact that the inflow velocity is not sensitive to δ, provided that the flow is magnetically dominated. In the above notation, $\hat{E}_{\rm EM}$ is the electromagnetic part of the total energy $\hat{E}$ (and the fluid part is $\hat{E}_{\rm FL} = \hat{E} - \hat{E}_{\rm EM} = u_t$).

At the stagnation surface, it is a good approximation to adopt $\hat{E}_{\rm FL} = u_t(r = r_s) \approx 1$ (the specific fluid energy is roughly equal to its rest-mass energy); therefore, we have

$$\hat{E}^-(\Psi) = 1 + \hat{E}^-_{\rm EM} < 0 \tag{21}$$

and

$$\hat{E}^+(\Psi) = 1 + \hat{E}^+_{\rm EM} > 0 \tag{22}$$

for the inflow and outflow solutions near $r = r_s$, respectively.

For the simple and straightforward case $\delta = 1$ and $\hat{E}^+_{\rm EM} \approx -\hat{E}^-_{\rm EM}$ (Pu et al. 2015), the following useful matching condition for the outflow and inflow solutions is obtained:

$$\hat{E}^-(\Psi) = 2 - \hat{E}^+(\Psi). \tag{23}$$

To satisfy Equation (19), the value of C in Equation (17) can then be specified by Equations (15), (17), and (23). The extraction of black hole rotational energy (by the $\hat{E}^-(\Psi) < 0$ flows) implies a minimal outflow energy

$$\hat{E}^+(\Psi) > 2. \tag{24}$$

[6] Recall that $(\hat{E}(\Psi), \hat{L}(\Psi))$ can be alternatively determined by $(r_s(\Psi), r_A(\Psi))$ in the cold limit. If any two of the four parameters in these pairs are known, the other two parameters are also known.

With known E^- and ξ^-, similar to the outflow case, it is sufficient to solve the Mach number and the poloidal velocity of the inflow, as described in Equation (11). A flowchart for the above procedure is presented and discussed in Appendix A.

2.6. Flow Velocity

The approximate flow velocity components u^r and u^θ can be obtained by the relation

$$\frac{u^r}{F_{\theta\phi}} = \frac{u^\theta}{F_{r\phi}}, \tag{25}$$

together with the definition of the poloidal velocity u_p.

The rest of the components of the four-velocity, u^t and u^ϕ, are obtained by the relation of

$$u_t + \Omega_F u_\phi = \hat{E} - \Omega_F \hat{L}, \tag{26}$$

together with

$$u^\alpha u_\alpha = 1. \tag{27}$$

Once the four-velocity of the flow is obtained, the magnetization parameter

$$\sigma(r; \Psi) \equiv \frac{\hat{E}_{\rm EM}}{\hat{E}_{\rm FL}} = \frac{\hat{E}(\Psi) - \hat{E}_{\rm FL}}{\hat{E}_{\rm FL}} = \frac{\hat{E}(\Psi) - u_t}{u_t} \tag{28}$$

is also determined with $\hat{E}_{\rm FL} = u_t$. The profile of $\sigma(\Psi; r)$ is associated with the energy conversion from $\hat{E}_{\rm EM}$ to $\hat{E}_{\rm FL}$ and therefore the flow acceleration efficiency. The initial magnetization at the stagnation surface has a good approximation with the flow energy of the outflow by

$$\sigma_s \equiv \sigma(r_s; \Psi) \approx \hat{E}_{\rm EM} \approx \hat{E}^+(\Psi), \tag{29}$$

because $\hat{E}_{\rm FL}(r = r_s) \approx 1$.

For an efficient acceleration, at large scale, $\sigma(r \to \infty) = \sigma_\infty \approx 0$, and the terminal Lorentz factor of the jet $\gamma(r \to \infty) = \gamma_\infty \approx \hat{E}^+(\Psi)$. Here we define the jet Lorentz factor, including the gravitational redshift factor of the outflow, by (e.g., McKinney 2006)

$$\gamma \equiv \sqrt{g_{tt}} u^t. \tag{30}$$

It is intriguing to note that, from Equations (8)–(15), for a specific field line, a faster outflow (a large value of γ and therefore $\hat{E}^+$) corresponds to a increase of pitch angle (a smaller value of β) at the stagnation surface.

2.7. Field Strength

As the deformation of the magnetic field due to mass loading is ignored, the flow solution is constructed by only three of the four streamline conserved quantities, $\Omega_F(\Psi)$, $\hat{E}(\Psi)$, and $\hat{L}(\Psi)$ (see also Appendix A), and the fourth conserved quantity, $\eta(\Psi)$, does not affect the resulting flow solution. For a given free function $\eta(\Psi)$, the magnetic field components have the form

$$\bar{B}_p(r; \Psi) = b_0 \frac{u_p}{M^2} \eta(\Psi), \tag{31}$$

$$\bar{B}_\phi(r; \Psi) = \beta(r; \Psi) \bar{B}_p(r; \Psi), \tag{32}$$

where b_0 is a free normalization parameter. Equations (31) and (32) also provide another way to understand our matching condition for the inflow and outflow solutions along the same

magnetic field line. Provided that both poloidal and toroidal magnetic fields are smooth and continuous at the stagnation surface r_s, we simply require a smooth and continuous behavior of β and η there. Accordingly, we have $\xi^-(r_s;\Psi)=\xi^+(r_s;\Psi)$, Equation (19), and $\eta^-(\Psi)\cong\eta^+(\Psi)$ (i.e., $\delta\cong 1$) at r_s, as described in Section 2.5. To avoid the singular behavior $u^r\to 0$ as $r\to r_s$, in practice, an interpolation of $\bar{B}_p(r\to r_s;\Psi)$ near $r=r_s$ can be applied to obtain the ratio between $\eta^-(\Psi)$ and $\eta^+(\Psi)$. One can also numerically verify that $\delta\cong 1$ can be consistently obtained when the energy matching condition, Equation (23), is adopted.

The number density in both the inflow and outflow regions can be obtained by the continuity relation

$$n=n_0\frac{\bar{B}_p}{u_p}\eta(\Psi)=\bar{n}_0\frac{\eta(\Psi)^2}{M^2}, \tag{33}$$

where $\bar{n}_0=4\pi\mu^2 n_0$ is a constant for the normalization.

3. Model Parameters

Our semianalytical model provides a flexible way to explore the parameter space of the black hole spin a, magnetic field configuration $\Psi(p)$, field angular velocity $\Omega_F(\Psi)$, and outflow energy $\hat{E}^+(\Psi)$.

We consider two qualitatively different functions of $\Omega_F(\Psi)$. The first is a constant field angular velocity, which is applied to both the parabolic and monopole fields,

$$\frac{\Omega_F}{\Omega_{\rm H}}=0.5, \tag{34}$$

where $\Omega_{\rm H}=a/(2r_{\rm H})$ is the magnetic field angular velocity and $r_{\rm H}=1+\sqrt{1-a^2}$ is the horizon radius. The second is a nonconstant distribution of the magnetic field angular velocity Ω_F (Blandford & Znajek 1977; McKinney & Narayan 2007; Beskin 2009) applied to the parabolic fields,

$$\frac{\Omega_F}{\Omega_{\rm H}}=\frac{\sin^2\theta_{\rm H}[1+\ln\mathcal{G}]}{4\ln 2+\sin^2\theta_{\rm H}+[\sin^2\theta_{\rm H}-2\mathcal{G}]\ln\mathcal{G}}, \tag{35}$$

where $\mathcal{G}=(1+\cos\theta_{\rm H})$. The profiles of the two field angular velocities as a function of penetrated horizon latitudes are plotted in Figure 1. For the nonconstant field angular velocity, the value varies from $\Omega_F=0.5\Omega_{\rm H}$ for $\theta_{\rm H}=0$ to $\Omega_F\approx 0.265\Omega_{\rm H}$ for $\theta_{\rm H}=\pi/2$.

In the following, we present flow solutions along parabolic magnetic field lines ($p=1$) in Section 4 and split-monopole magnetic field lines ($p=0$) in Section 5.

4. Trans-fast Magnetosonic Flow along Parabolic Magnetic Field Lines

4.1. Example of Solutions along a Magnetic Field Line

To demonstrate our semianalytical approach, let us start with flow solutions along one single magnetic field line. In Figure 2, the solutions for the flow along a magnetic field line with $\Omega_F=0.5\Omega_{\rm H}$ and $\theta_{\rm H}=85^\circ$ of a spinning black hole $a=0.95$ are shown. The solid and dashed profiles corresponds to two different boundary conditions, $\hat{E}^+=10$ and 100, respectively. Note that the corresponding $\hat{L}^+$ are uniquely determined with the given $\hat{E}^+$ and Ω_F (see Section 2.4). For this specific setup, $\hat{L}^+\simeq 52.2$ for $\hat{E}^+=10$, and $\hat{L}^+\simeq 549.4$ for $\hat{E}^+=100$.

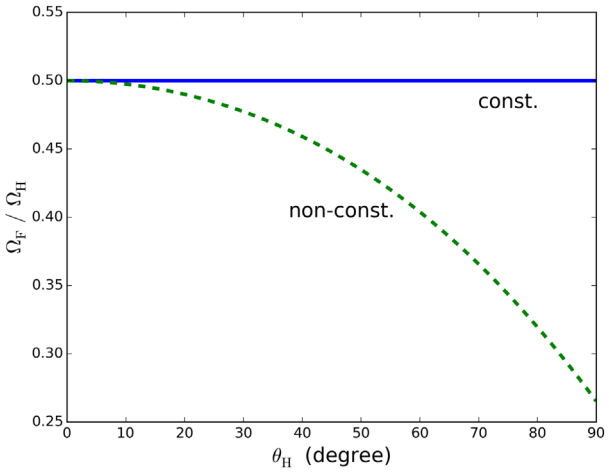

Figure 1. Possible profiles of the angular velocity of magnetic fields Ω_F vs. polar angle on the black hole event horizon $\theta_{\rm H}$ in terms of the angular velocity of the hole $\Omega_{\rm H}$: constant field angular velocity (solid line; Equation (34)) and nonconstant field angular velocity (dashed line; Equation (35)).

The square of the Mach number M^2, which is a solution of Equation (11) for $\hat{E}=(10, 100)$, is shown in the top panel of Figure 2. The resulting pitch angles by the matching condition introduced in Section 2, as plotted in the second panel, roughly follow the criteria of the kink instability, $(B^r/B^\phi)\approx(1/g_{\phi\phi}\Omega_F)$ (Tomimatsu et al. 2001), consistent with the results of the GRMHD simulation (McKinney 2006) and semianalytical computations (Pu et al. 2015). For the outflow, the poloidal and toroidal components of the magnetic field become comparable ($\beta\approx 1$) near the outer light surface (yellow vertical line in the outflow region). This is a well-known property of a magnetically dominated MHD flow. The components of the flow four-velocity are shown in the bottom panel of Figure 2. Note that the flow four-velocity of the two solutions has noticeable differences only at the larger scale ($r>100r_g$ in the plot). For the inflow, as discussed in Pu et al. (2015), the four-velocity of a magnetically dominated inflow is not sensitive to the flow energy because the Alfvén surfaces are always located close to the inner light surface and the FMS is always located close to the horizon, as will be shown in Section 4.3. These characteristic surfaces will be shown later in this section.

The physical reason for the existence of the outer and inner light surfaces can also be recognized from the flow solution. To satisfy the requirement of causality, the outer surface marks the boundary beyond which the flow motion must be mostly poloidal, as can be seen by that $u^r>u^\phi$ beyond the outer light surface. The inner light surface, on the other hand, marks the boundary beyond which the flow is close enough to the central rotating black hole and must rotate faster due to the gravitational redshift effects. As we will also see in Section 4.3, close to the horizon, the flow corotates with the black hole.

4.2. Jet Acceleration and Energy Conversion

We now focus on the outflow region and examine the jet acceleration via the evolution of the jet Lorentz factor. Results of different black hole spin ($a=0.1, 0.5, 0.95$) and the total energy of the outflow ($\hat{E}^+=10, 100, 500$) are shown in Figure 3. Again, we focus on a field line that penetrates the black hole at $\theta_{\rm H}=85^\circ$ and assume $\Omega_F=0.5\Omega_{\rm H}$. The cases for $\hat{E}^+=10, 100$ and $a=0.95$ therefore correspond to the solutions shown in Figure 2. The Lorentz factor versus the

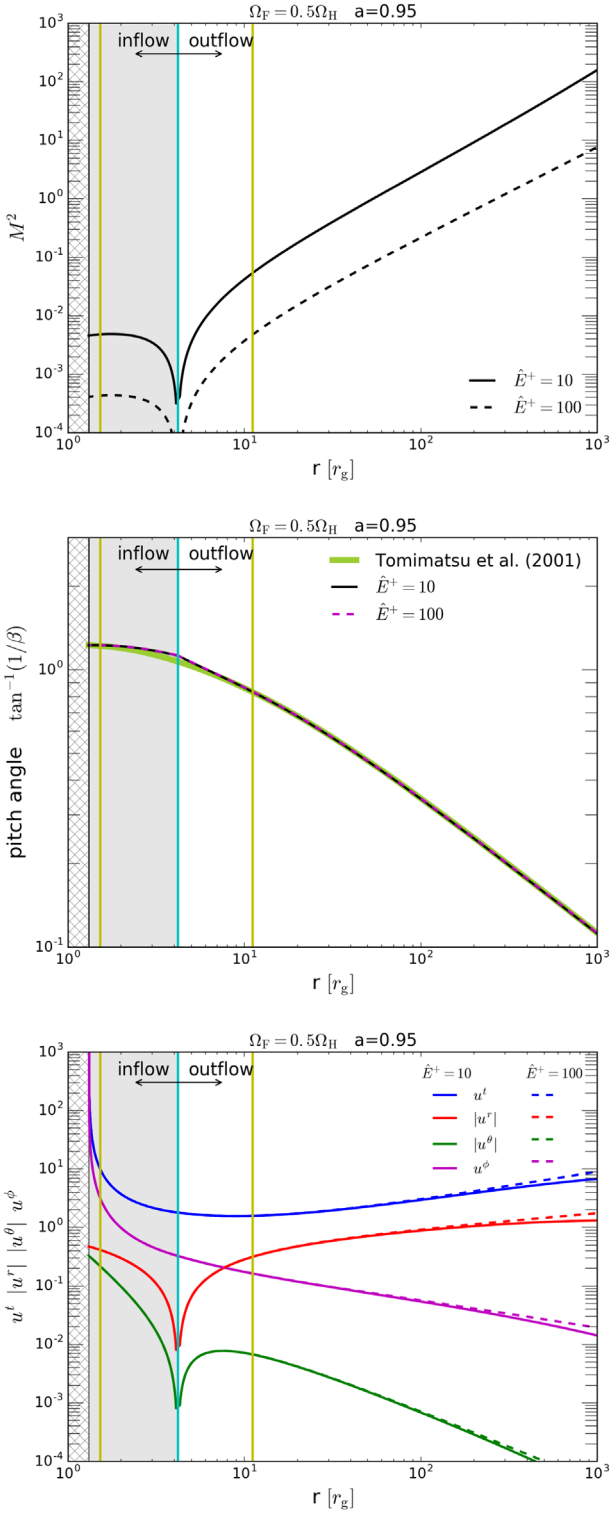

Figure 2. Example flow solutions of different outflow energy $\hat{E}^+$ along a parabolic magnetic field line ($\theta_H = 85°$) in the magnetosphere of a rotating black hole. Top panel: Mach number square M^2. Middle panel: pitch angle, which is well approximated by the profile $(1/g_{\phi\phi}\Omega_F)$, below which the kink instability takes place (Tomimatsu et al. 2001). Bottom panel: flow four-velocity u^α. The locations of the stagnation surface (cyan vertical line) and the inner/outer light surfaces (yellow vertical lines) are indicated. The shaded gray area indicates the inflow region, and the hatched area indicates the black hole.

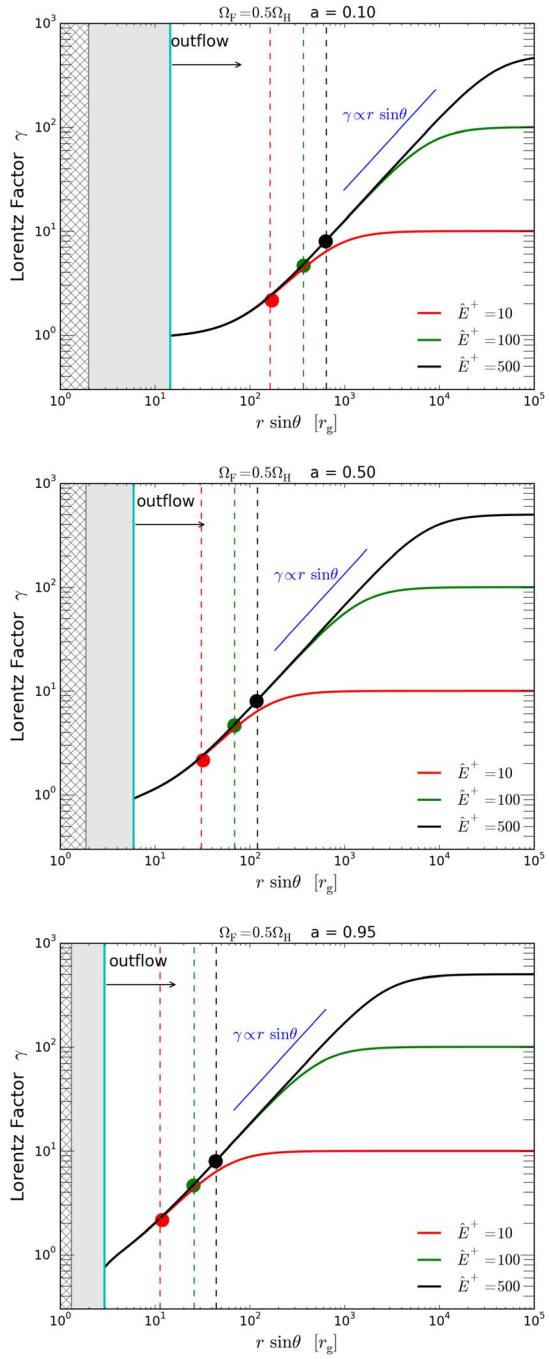

Figure 3. Lorentz factor of the GRMHD outflow γ vs. the distance away from the rotational axis ($\theta_H = 85°$) for cases of different outflow energy $\hat{E}^+$ and dimensionless black hole spin a. At large distances, $\gamma_\infty \approx \hat{E}^+$ due to the efficient conversion from electromagnetic to kinetic energy. The vertical dashed lines indicate the locations of the corresponding location of the FMS for each solution. The theoretical predicted location $((r\sin\theta)^{\rm SRMHD}_{\rm FMS} \approx (\hat{E}^+)^{1/3}/\Omega_F)$ and Lorentz factor $(\gamma^{\rm SRMHD}_{\rm FMS} \approx (\hat{E}^+)^{1/3})$ at the FMS for an SRMHD flow (TT03; Beskin & Nokhrina 2006) is overlapped by the colored circles, which roughly fits our GRMHD solution for the outflow. The inflow region is indicated by the shaded gray area. The hatched gray area indicates the black hole. See Section 4.2 for more discussion.

distance away from the black hole is computed only for the outflow solution; therefore, the profile starts from the stagnation surface (the cyan vertical line). The location of the stagnation surfaces moves further away from the black hole as the black hole spin becomes lower due to the resulting smaller Ω_F and therefore weaker magnetocentrifugal force applied to the plasma loading onto the magnetic field line. The location of the FMS for each flow solution is indicated by the vertical

dashed lines. For all cases, the γ profiles linearly grow ($\gamma \propto r\sin\theta$) in the superfast-magnetosonic region until the flow reaches a value $\gamma \approx \hat{E}^{+}$.

By examining the perturbation on the equation of motion for the plasma outflow in a parabolic force-free field line[7] $\Psi_0 \propto r(1-\cos\theta)$ in flat spacetime, Beskin & Nokhrina (2006) found that the flow Lorentz factor grows with the distance $z = r\cos\theta$ from the equatorial plane with[8] $\gamma \propto z^{1/2}$ until the flow converts all of its electromagnetic energy into kinetic energy. In addition, the FMS is located at $(r\sin\theta)_{\rm F}^{\rm SRMHD} \approx \sigma_0^{1/3}/\Omega_F$, and the Lorentz factor there is $\gamma_{\rm F}^{\rm SRMHD} \approx \sigma_0^{1/3}$, where σ_0 is Michel's magnetization parameter (Michel 1969). The same conclusion is also obtained in TT03 (2003).

To compare with SRMHD theory in the distant flat spacetime, the above predicted location and Lorentz factor at the FMS are overlapped in Figure 3 (colored circles) by considering the magnetization at the stagnation surface, where the outflow starts: $\sigma_{\rm s} \approx \hat{E}^{+}$ (see also Equation (29)). A good agreement of the jet acceleration between SRMHD and GRMHD flows for all different black hole spins is found. Such interesting features seem to result from the fact that the outflow region is far enough away from the black hole.

To show the energy conversion from the electromagnetic component $\hat{E}_{\rm EM}$ to the fluid component $\hat{E}_{\rm FL}$ along the flow, the ratio of the two components, σ, is shown in Figure 4. The inflow part is also shown in the plot, but note that $\hat{E}_{\rm EM} < 0$ (and $\hat{E}_{\rm FL} > 0$) in the inflow region (see also Pu et al. 2015), and the black hole rotational energy is extracted by an outgoing Poynting flux-dominated GRMHD inflow that has a negative total energy ($\hat{E} = \hat{E}_{\rm EM} + \hat{E}_{\rm FL} < 0$; Takahashi et al. 1990). The energy conversion for the outflow starts from $\sigma_{\rm s} \approx \hat{E}^{+}$ at the stagnation surface and gradually decreases when the $\hat{E}_{\rm EM}$ component converts to $\hat{E}_{\rm FL}$. It is clearly shown that the flow remains Poynting flux-dominated at the FMS. The energy conversion efficiency at the FMS is again consistent with the predicted value from magnetically dominated SRMHD flows (TT03 2003; Beskin & Nokhrina 2006), $\sigma_{\rm FMS}^{\rm SRMHD} \approx (\hat{E}^{+})^{1/3}$, as indicated by the colored circles in Figure 4.

We further consider cases of different field angular velocity in Figure 5, with fixed outflow energy $\hat{E} = 100$ and black hole spin $a = 0.5$. While the decrease of the angular velocity results in closer stagnation surfaces (indicated by stars) and location of the FMS (indicated by dashed vertical lines), the resulting flow solutions are also in good agreement with the predicted values from magnetically dominated SRMHD flows (TT03; Beskin & Nokhrina 2006).

4.3. Jet Properties near the Black Hole

The global properties of a GRMHD jet near a black hole can be examined by solving the trans-fast magnetosonic solutions for the whole magnetic field lines within the funnel region. The

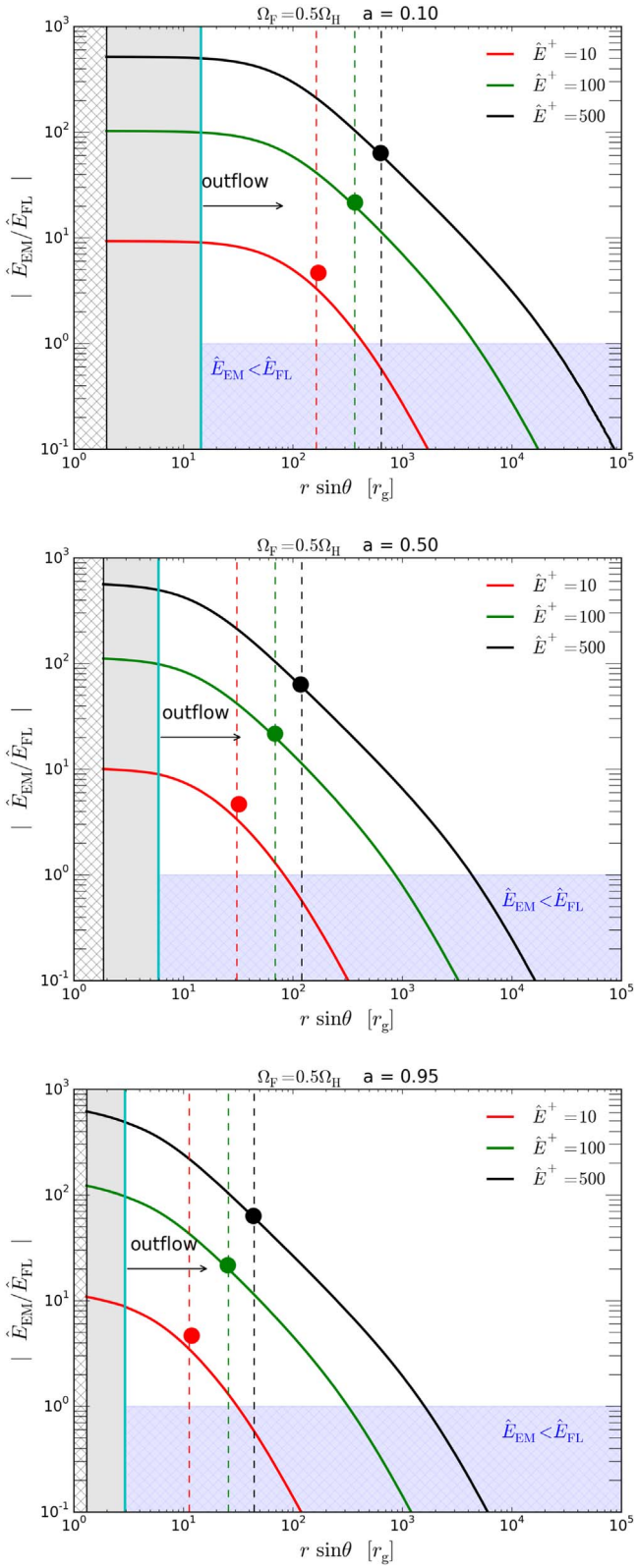

Figure 4. Conversion from the electromagnetic energy $\hat{E}_{\rm EM}$ to the fluid energy $\hat{E}_{\rm FL}$ of both the outflow solutions shown in Figure 3 and their corresponding inflow solutions. The vertical dashed lines indicate the locations of the corresponding location of the FMS for each solution. The theoretical predicted location and the energy conversion efficiency ($\sigma_{\rm FMS}^{\rm SRMHD} \approx (\hat{E}^{+})^{2/3}$) at the FMS for an SRMHD flow are overlapped by the colored circles, which roughly fits our GRMHD solution for the outflow. The inflow region is indicated by the shaded gray area, and the hatched gray area indicates the black hole. In the hatched blue area, $\hat{E}_{\rm EM} < \hat{E}_{\rm FL}$.

[7] The unperturbed field Ψ_0 considered in Beskin & Nokhrina (2006) has the form $\Psi_0 \propto \ln[\Omega_F X + \sqrt{(\Omega_F X)^2+1}\,]$, where $X = r(1-\cos\theta)$. By using the relation $\sinh^{-1}(x) = \ln(x+\sqrt{x^2+1}\,)$, the dominant form of Ψ_0 is found to be $r(1-\cos\theta)$.

[8] For a magnetic field $\Psi \propto r^p(1-\cos\theta)$, the magnetic field line shape $z \propto (r\sin\theta)^{2/(2-p)}$ (see, e.g., Tchekhovskoy et al. 2008). For $p = 1$, the relation $\gamma \propto z^{1/2}$ is consistent with our outflow solutions shown in Figure 3, which satisfy $\gamma \propto r\sin\theta$.

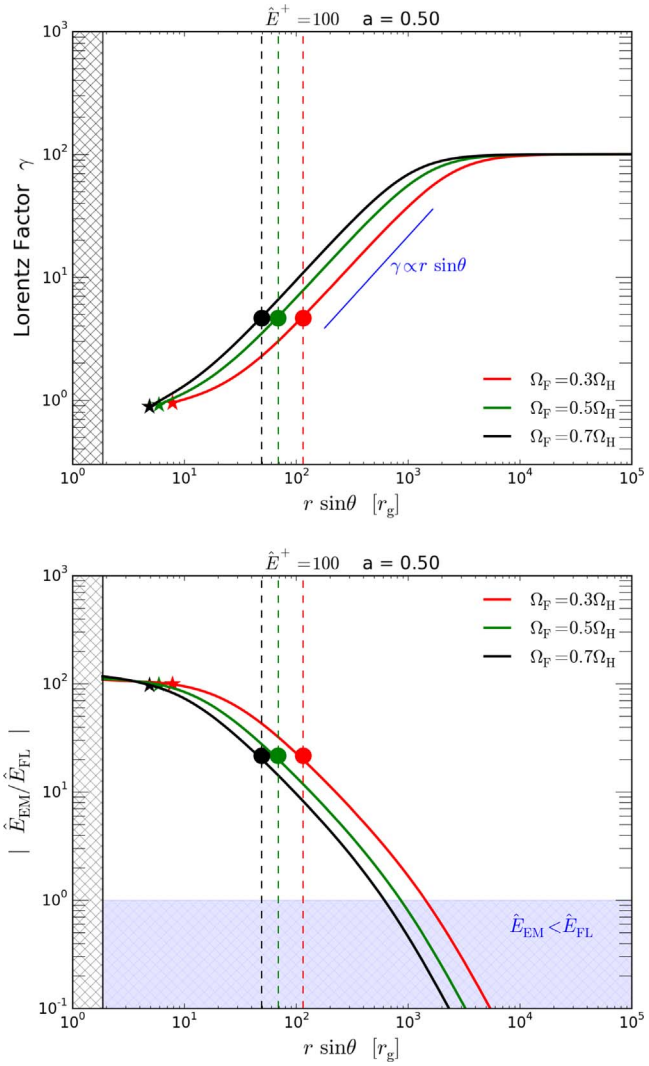

Figure 5. Lorentz factor of the outflow (top) and energy conversion (bottom) of flows along magnetic fields with different field angular velocities. The locations of the stagnation surfaces are indicated by stars. See also Figures 3 and 4 for explanations of the plot.

GRMHD jet solutions in the black hole magnetosphere with a constant magnetic field angular velocity are shown in Figure 6 for the case $\hat{E}(\Psi) = 10$ and black hole spins $a = 0.5$ (top) and 0.95 (bottom). The flow boundary shown here corresponds to the flow along the magnetic field line that penetrates the event horizon at $\theta_H = 90°$. For all panels, the stagnation surface (dashed white line), outer light surface (solid white line), outer Alfvén (dashed red line), and outer FMS (solid red line) are plotted. As shown in the inset of the left panels, the inner Alfvén and FMSs are located inside the static limit surface, satisfying the necessary condition to extract black hole rotational energy outward (Takahashi et al. 1990). For a Poynting flux-dominated flow, the Alfvén surfaces almost coincide with the light surfaces, and the inner FMS almost coincides with the event horizon, as seen in both the top and bottom panels. As also seen in Figure 3, the stagnation surface of a faster-spinning black hole is located closer to the central black hole.

The ratio of the toroidal and poloidal components of the magnetic field are shown in the left panels of Figure 6. As shown in the plot, the poloidal field dominates in the inflow region and close to the rotational axis and becomes comparable to the toroidal magnetic field near the outer Alfvén surface.

In the middle panels of Figure 6, the poloidal three-velocity square, $v_p^2 \equiv (u_p/u^t)^2$, is shown. The stagnation surface ($u^r = 0$ and $u^\theta = 0$) separates the inflow region ($u^r < 0$ and $u^\theta > 0$) and the outflow region ($u^r > 0$ and $u^\theta < 0$). Along the magnetic field line, for the inflow, v_p is not monotonic; the flow three-velocity gradually increases after they departure from the stagnation surface, but drops quickly before they enter the black hole due to the rapid increase of u^t near the black hole (see also the bottom panel of Figure 2). For the outflow, v_p continuously increases.

We show the angular velocity of the flow, $\Omega = u^\phi/u^t$, in the right panels of Figure 6. Note that $\Omega(\Psi) \approx \Omega_F(\Psi)$ at the stagnation surface due to the vanishing poloidal velocity there. For the inflow, Ω gradually increases when it streams toward to the black hole; finally, $\Omega(\Psi) \approx \Omega_H$ due to the black hole rotation.

In Figure 7, we plot the properties of the GRMHD jet with the magnetic field with the nonconstant angular velocity. In addition to the fact that the flow also shares the above-mentioned general flow features shown in Figure 6, the locations of the stagnation surfaces in Figure 7 move further away from the black hole due to a slower field angular velocity profile (see also Figure 1). It is interesting to note that a more rapid decrease of $\Omega_F(\Psi)$ near the jet boundary results in the "V shape" of the stagnation surfaces, with its valley located close to the jet boundary. Such a V shape of the stagnation surfaces in turn modifies the profile of the outer light surface and therefore the outer Alfvén surface. Note how the resulting constant v_p^2 contours (middle panels) also have a V-shaped profile, indicating a nonmonotonic "slow–fast–slow" structure of the jet Lorentz factor across the jet. The outer slow layer adjacent to the funnel results from the differential rotation in the magnetosphere of a spinning black hole instead of a slower wind region emerging from the corona of the accretion flow. The resulting effect on the radiative transfer from the noticeable difference in velocity between a constant and nonconstant field angular velocity (while keeping all other parameters the same), as seen in the insets of Figures 6 and 7, may, in principle, be distinguishable by horizon-scale black hole images or movies (e.g., Jeter et al. 2018). The first black hole image was recently obtained by the Event Horizon Telescope (Event Horizon Telescope Collaboration et al. 2019a, 2019b, 2019c, 2019d, 2019e, 2019f). In addition, if energetic electrons are continuously or intermittently injected from the stagnation surface, its location could be constrained by horizon-scale observations (e.g., Pu et al. 2017).

4.4. Characteristic Surfaces

To present the distribution of characteristic surfaces—stagnation, inner/outer Alfvén, and inner/outer FMS—we plot in Figure 8 the result of three different outflow energies, $\gamma_\infty \approx \hat{E}^+(\Psi) = (10, 100, 500)$, in a constant (left panel) and differential (right panel) black hole magnetosphere with $a = 0.95$. The case for $\hat{E}^+ = 10$ corresponds to the solutions shown in the bottom panels of Figures 6 and 7. The location of the stagnation surface (cyan) and inner/outer light surfaces (yellow) are strongly related to $\Omega_F(\Psi)$ and independent of $\hat{E}^+$. Because the resulting locations of the inner FMSs (which almost coincide with the event horizon) and inner/outer Alfvén

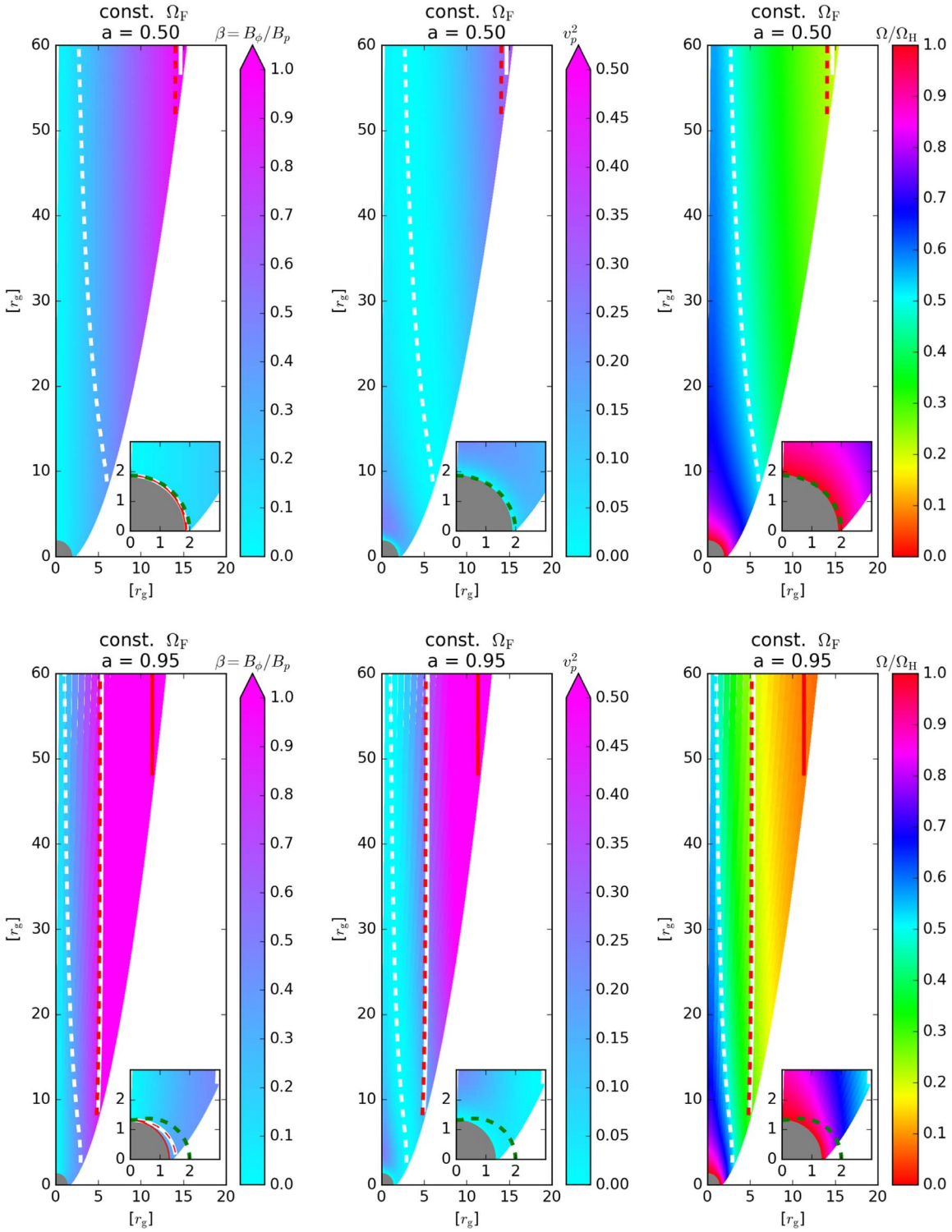

Figure 6. GRMHD flow structure of a parabolic magnetosphere with a constant field angular velocity $\Omega_F(\Psi) = 0.5\Omega_{\rm H}$ for cases of different dimensionless black hole spin a. The total energy of the outflow is assumed to be $E^+(\Psi) = 10$. Left panels: β, the ratio between the toroidal and poloidal magnetic fields. Middle panels: square of the poloidal flow velocity $v_p^2 \equiv u_p^2/(u^t)^2$. Right panels: angular velocity of the flow $\Omega \equiv u^\phi/u^t$, in terms of black hole angular velocity $\Omega_{\rm H}$. For all panels, the outer FMS (solid red line), outer light surface (solid white line), outer Alfvén surface (dashed red line), and stagnation surface (dashed white line) are shown. The static limit surface is indicated by the green dashed line in the insets. The inner light surface (solid white line), inner Alfvén surface (dashed red line, which almost coincides with the solid white line), and inner FMS (solid red line) are shown in the inset of the left panels. The central shaded area indicates the black hole. See Section 4.3 for more discussion.

surfaces (which almost coincide with the inner/outer light surfaces) are all similar for all different $\hat{E}^+$ considered here, we only show the locations of these surfaces for the case of $\hat{E}^+(\Psi) = 10$ (red). The outer FMSs for different $\hat{E}^+(\Psi)$, which relate closely to the jet acceleration process (as discussed in Section 4.2), are shown by the solid lines in different colors. In general, the location of the FMS of the outflow moves further away from the black hole for a larger $\hat{E}^+$. The resulting V

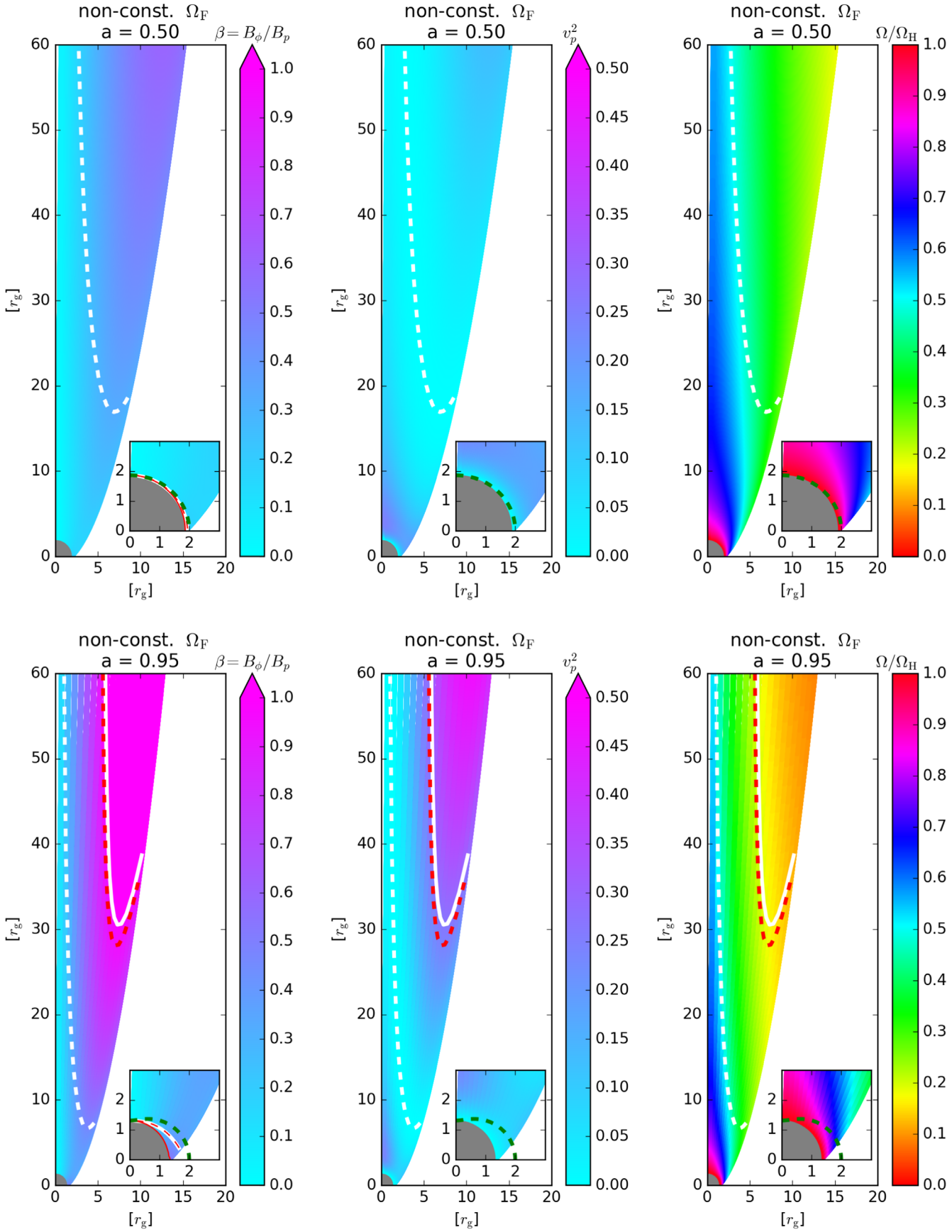

Figure 7. Same as Figure 6 but for the cases of the nonconstant field angular velocity profile $\Omega_F(\Psi)$ shown in Figure 1.

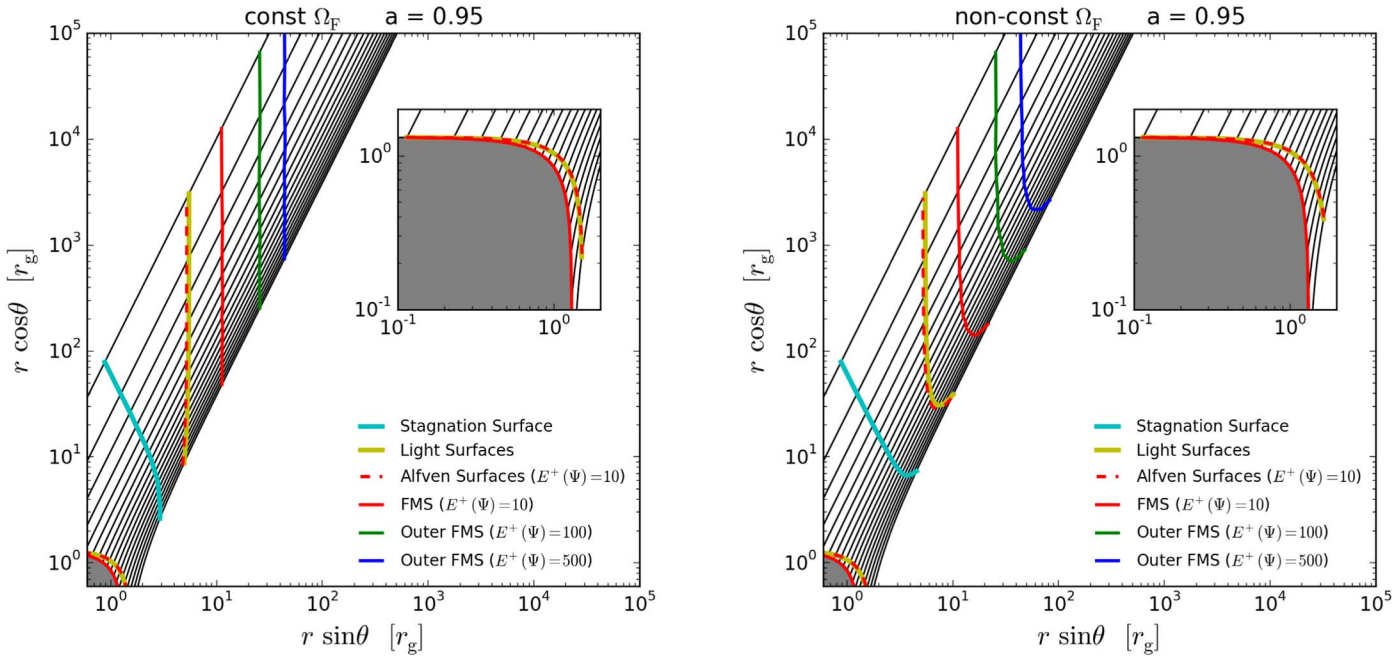

Figure 8. Characteristic surfaces of a parabolic magnetosphere with constant and nonconstant field angular velocities (Figure 1) around a fast-spinning black hole, $a = 0.95$. The inner and outer light and stagnation surfaces are shown by the yellow and cyan lines, respectively. The outer FMSs for the total energy of outflow $E^+(\Psi) = (10, 100, 500)$ are shown by the solid lines in different colors. The black hole is indicated by the gray shaded region. The inner fast surfaces of all different $E^+(\Psi)$ almost coincide with the event horizon. In this plot, the outermost and innermost field lines attach to the horizon at $\theta_H = 90°$ and 5°, respectively. See Section 4.4 for more discussion.

shapes of the stagnation surface and outer Alfvén and FMS for a differential $\Omega_F(\Psi)$ (right panel) are also clearly shown.

While the surfaces shown in Figure 8 correspond to constant $\hat{E}^+(\Psi)$, the case for nonconstant $\hat{E}^+(\Psi)$ distribution can be qualitatively inferred by the combination of the locus of different $\hat{E}^+(\Psi)$ at different Ψ. For example, for the GRMHD simulation of an accreting black hole system with $a = 0.9375$ presented in McKinney (2006), the velocity at the jet core is slower compared to the jet boundaries. By linking the surfaces with a higher outflow energy $\hat{E}^+ \sim 100$ near the jet boundary to a lower outflow energy $\hat{E}^+ < 100$ toward to the core (the jet axis direction), the resulting profiles of the Alfvén and FMSs thus have a concave profile bending toward to the jet axis, qualitatively explaining the result of McKinney (2006), in which the locus of the FMS gradually becomes horizontal near the pole region in a log–log plot (Figure 11 of McKinney 2006).

Recently, notes have been added to the result of McKinney (2006). Chatterjee et al. (2019) performed a number of large-scale simulations with $a = 0.9375$ and compared with the result of McKinney (2006). In general, the overall characteristic surfaces shown in Figure 14 of Chatterjee et al. (2019) are similar to those in Figure 11 of McKinney (2006). Intriguingly, the surfaces show V shape–like profiles, a similar feature as shown in the right panel of Figure 8. They also found that the pinch instabilities of the magnetic field developed around the boundary layer region between the jet and the surrounding wind/corona region play an important role in converting electromagnetic energy into heat energy. Although we assume the magnetic field configuration by the parameter p, the GRMHD simulations indicate that the field geometry mildly deviates from the parabolic magnetic field line of $p = 1$ (e.g., Figure 11 of McKinney 2006 and Figure 14 of Chatterjee et al. 2019). Note that, in our model of cold GRMHD flow, the slow-magnetosonic speed is zero everywhere. In contrast, the pressure of the flow is properly considered in the GRMHD simulation, and therefore the slow-magnetosonic surface appears. The location of the stagnation surface would vary from the cold fluid limit we considered here, depending on the thermodynamical properties of the plasma (e.g., the electron temperature). Nevertheless, as the thermodynamical properties have little effect on jet acceleration, except when the pitch effect takes place, our semianalytical model for the cold flow is capable of providing qualitative and (rough) quantitative insights into a magnetically dominated GRMHD flow structure from the horizon to a large distance. Observationally, for a black hole system with known jet acceleration across the jet cross section at a different radius, the black hole spin and the characteristic surfaces may therefore be constrained (see, e.g., Nakamura et al. 2018, for the case of M87).

5. Trans-fast Magnetosonic Flow along Split-monopole Magnetic Field Lines

We now explore the split-monopole magnetosphere ($p = 0$). Motivated by the SRMHD flow for different plasma loading across field lines (Tchekhovskoy et al. 2009), here we also release the assumption of a constant $\hat{E}^+(\Psi)$ and choose three representative different profiles by

$$\hat{E}^+(\Psi;\, \theta_H) = \hat{E}_{\max} \sin^{\chi}(\kappa\theta_H) + \hat{E}_{\min}, \tag{36}$$

where $\hat{E}_{\max}$ and $\hat{E}_{\min}$ are the maximum and minimal energy, and χ and κ are the parameters controlling the corresponding angle when $\hat{E}(\Psi;\, \theta_H) = \hat{E}_{\max}$. Here we adopt $\hat{E}_{\max} = 460$ and $\hat{E}_{\min} = 10$.

We consider three different energy distributions of $\hat{E}^+(\Psi)$, as shown in Figure 9. For case A, for reference, we adopt a constant $\hat{E}^+(\Psi)$ across the magnetosphere, with $\chi = 0$. For

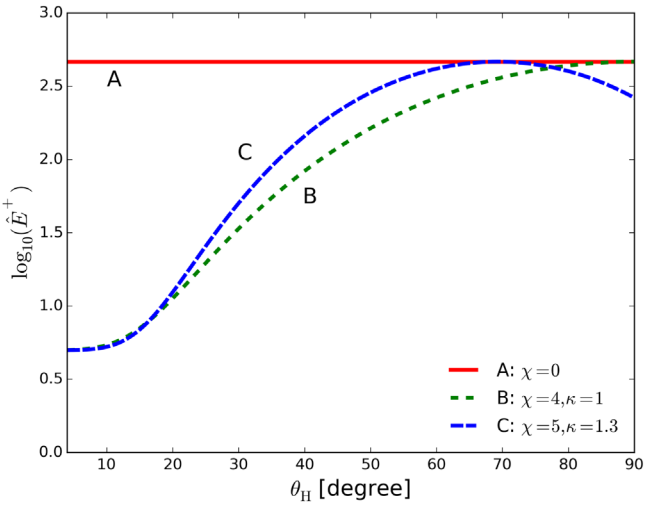

Figure 9. Three different cases of the outflow energy $\hat{E}^+(\Psi)$ along a split-monopole magnetic field line that penetrates the event horizon at different polar coordinates $\theta_{\rm H}$. See Section 5 for more details.

case B, by adopting $\chi = 4$ and $\kappa = 1$, a monotonically increasing $\hat{E}^+ = \hat{E}_{\rm min}$ from the pole region then reaches $\hat{E}_{\rm max}$ at the funnel region of the accreting gas (the jet boundary). For case C, the $\hat{E}^+$ reaches $\hat{E}_{\rm max}$ at around $\theta_{\rm H} \sim 70°$, then deceases toward the jet boundary, as described by using $\chi = 5$ and $\kappa = 1.3$. The constant field angular velocity, Equation (34), is applied for the split-monopole magnetic configuration considered here (Blandford & Znajek 1977; Phinney 1983). However, among the three representative cases, A, B, and C, the last case seems more physical (see also Tchekhovskoy et al. 2009).

As in Tchekhovskoy et al. (2009), it seems convenient to show the Lorentz factor γ in the "logarithmic" spherical coordinate. In Figure 10, we consider a black hole with $a = 0.5$ and present the Lorentz factor of the GRMHD outflows. The shapes of the stagnation surface (cyan lines), inner and outer light surfaces (yellow lines), and outer Alfvén surface and FMS (dashed and solid red lines, respectively) are all elongated in the direction toward the polar direction. We should note that the efficient energy conversion is not efficient for a split-monopole configuration (see Tchekhovskoy et al. 2009), and the efficient jet acceleration (i.e., $\gamma \to \hat{E}^+(\Psi)$) far away from the FMSs is artificial due to the assumption for the parameter ζ_0 (see also Section 3 and Appendix B). Therefore, the region far away from the outer FMS for a split-monopole configuration is beyond our interest and approach.

The perturbation on the equation of motion for the plasma loading onto a split-monopole force-free magnetic field line $\Psi \propto (1 - \cos\theta)$ in flat spacetime was well studied in Beskin et al. (1998). The authors found that the FMS is located at[9] $(r\sin\theta)^{\rm SRMHD}_{\rm FMS} \approx \sigma_0^{1/3}/\Omega_F$ and the Lorentz factor there is $\gamma^{\rm SRMHD}_{\rm FMS} \approx \sigma_0^{1/3}$, where σ_0 is Michel's magnetization parameter (Michel 1969). The comparison between our GRMHD solutions and the above predicted properties is shown in Figure 11. The green circles represent the location computed by $(r\sin\theta)^{\rm SRMHD}_{\rm FMS} \approx (\hat{E}^+)^{1/3}/\Omega_F$, which shows good agreement with the FMS locations of the GRMHD outflow solutions (solid red lines). It is also clear that, for a given magnetic field line, the location of the outer FMS is further away for a larger $\hat{E}^+$. Therefore, different choice of $\hat{E}^+(\Psi)$ correspondingly result in different profiles of the FMS. The color map in Figure 11 shows the magnetization. It is verified by the contour $\sigma/(\hat{E}^+)^{2/3} = 1$ that $\gamma^{\rm SRMHD}_{\rm FMS} \approx (\hat{E}^+)^{1/3}$ is a good approximation of the energy conversion ratio at the FMS of the outgoing GRMHD flow.

[9] Although the transverse distance to the FMS, $(r\sin\theta)^{\rm SRMHD}_{\rm FMS} \approx \sigma_0^{1/3}/\Omega_F$, is the same for the split-monopole case (Beskin et al. 1998) and the parabolic field line case (Beskin & Nokhrina 2006), the radial distance to the FMS, $(r)^{\rm SRMHD}_{\rm FMS}$, is much shorter for the former case compared to the latter due to different field geometry.

6. Limitation of the Model

Although the presented semianalytical model provides a fast and intuitive way to explore the steady trans-fast magnetosonic outflow along magnetic field lines in the black hole magnetosphere, there are some limitations to this approach. Here we enumerate several cautions for the utility of our model.

In our outflow model, we assume a magnetically dominated black hole magnetosphere at the jet formation region, so that we apply the solution of force-free magnetic fields there by construction. The obtained trans-fast magnetosonic flow solution becomes fluid kinetic energy-dominated at the radius about 10 times the radius of the FMS, so that the effect of plasma inertia on the magnetic field shape cannot be ignored (e.g., TT03). In this case, it is necessary to evaluate the force-balance equation of the magnetic field lines, and our presented approach cannot be applied.

Another limitation is the flow solution close to the pole region, $\theta \to 0$. Such a region requires more cautions for several reasons. First, our model scheme applies for flow that passes the outer light surface. However, close to the rotational axis of the magnetosphere, the location of the outer light surface moves toward infinity ($r_L \gg 1$ for $\theta_L \ll 1$, where L denotes the outer light surface). Second, field lines near the pole tend to bunch up around the axis due to mass loading (e.g., Tchekhovskoy et al. 2009, 2010), which is beyond the application of our working assumption, since the deformation of the force-free field is completely ignored. In general, the flow energy, mass loading, and deformation of the magnetic field lines are all related (e.g., Pu et al. 2015).

7. Summary and Outlook

A semianalytical approach for modeling the global stationary trans-fast magnetosonic jet structure is presented in this paper by the following working assumptions: (i) adopting a prescribed poloidal force-free magnetic field configuration and ignoring the deformation of the fields due to the plasma loading and (ii) prescribing a sophisticated relation between the poloidal and toroidal components of the magnetic field (TT08) to preserve the key physics that resulted from the plasma inertia, including the jet acceleration and the existence of the FMS. The trans-fast magnetosonic outflow model by introducing a regular function $\beta(r; \Psi)$ thus easily integrates all the key processes for a black hole–powered jet acceleration at different scales from horizon ($\approx r_{\rm g}$) to large ($>10^{4-5} r_{\rm g}$; ~pc scale). We discuss GRMHD jet acceleration and magnetization along magnetic field lines in black hole magnetospheres. Then we show their dependence on the black hole spin a, magnetic field geometry Ψ, angular velocity of the magnetic field line $\Omega_F(\Psi)$, and total energy of the outflow $\hat{E}^+(\Psi)$.

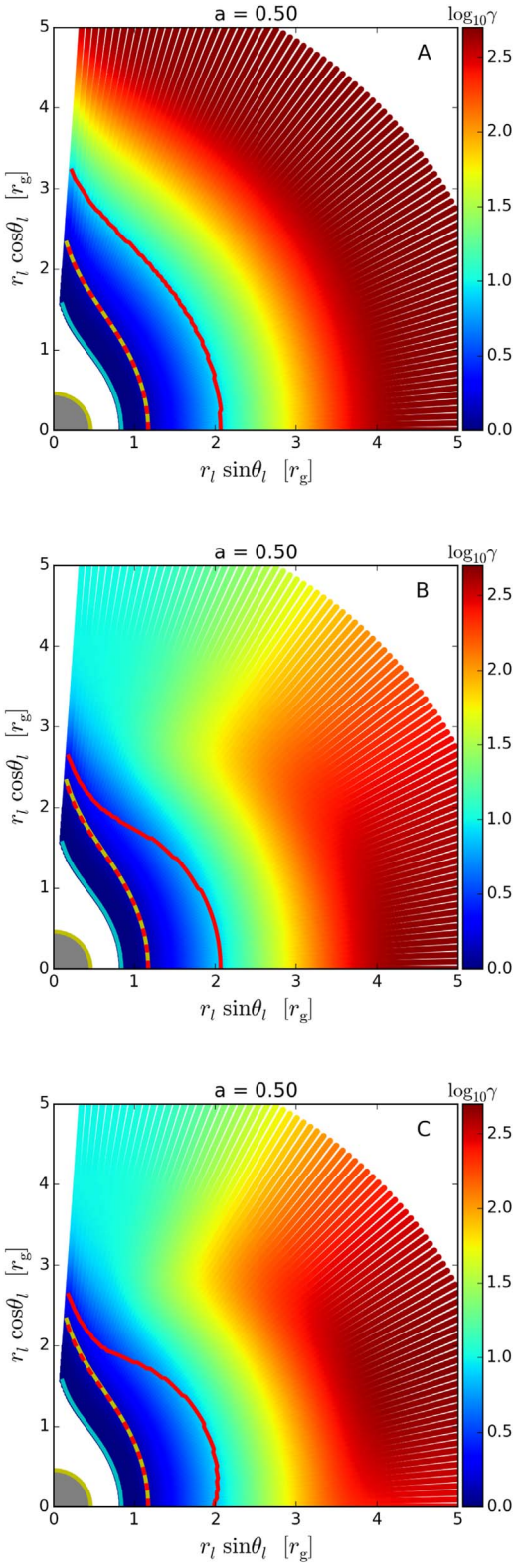

Figure 10. Lorentz factor of the GRMHD outflow along a split-monopole magnetosphere of a modest spinning black hole, $a = 0.5$, for the different flow energy choices shown in Figure 9: cases A (top panel), B (middle panel), and C (bottom panel). A "logarithmic" spherical coordinate (r_l, θ_l) defined by ($r_l = 1 + \log_{10}(r)$, $\theta_l = \theta$) is adopted. The light surfaces (yellow lines, which almost overlap with the red dashed lines) and stagnation surface (cyan lines) are shown. The central shaded area indicates the black hole. The inner dashed and outer solid red lines are the Alfvén surface and FMS of the outflow.

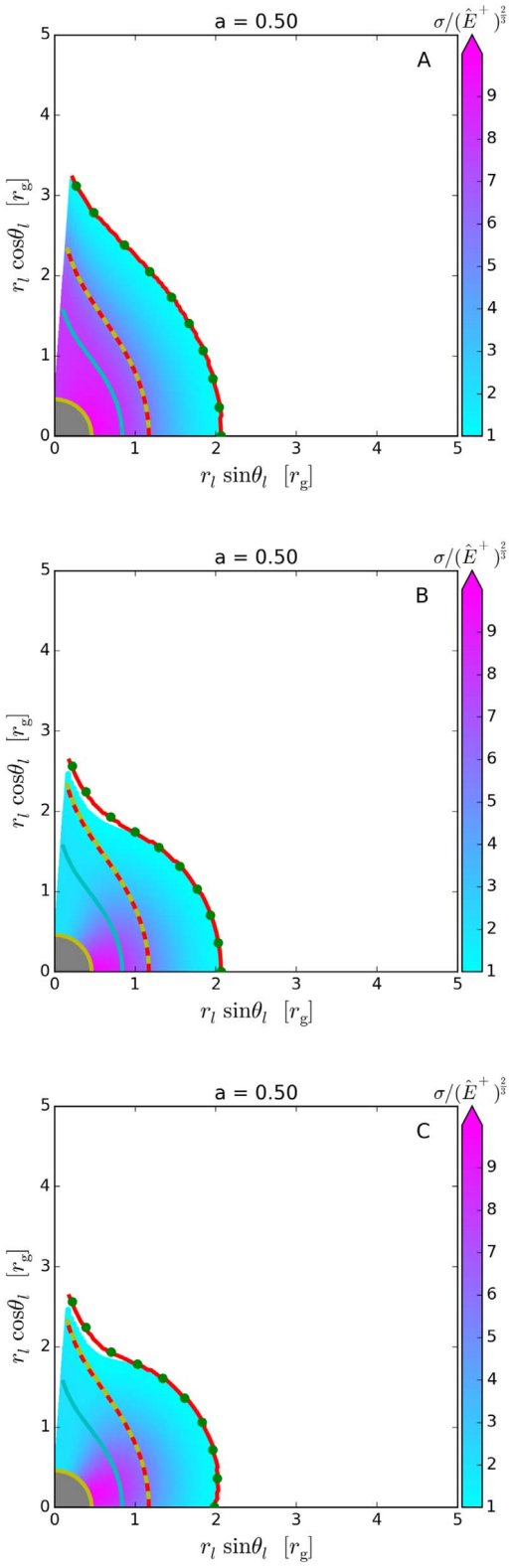

Figure 11. Corresponding magnetization, rescaled by $(\hat{E}^+)^{2/3}$, for both the outflow and inflow regions of Figure 10. Regions for $\sigma/(\hat{E}^+)^{2/3} < 1$ are not shown in order to highlight that contours of $\sigma/(\hat{E}^+)^{2/3} = 1$ roughly fit the outer FMS (outer red lines), consistent with the theoretical prediction for an SRMHD flow along a split-monopole case (Beskin et al. 1998). The green circles indicate the theoretical prediction location for selected field lines, which is also in good agreement with the location of the outer FMS.

The solution of our models includes the extraction of black hole rotational energy via the inflow, a continuous propagation of Poynting energy flux where the inflow and outflow matches the plasma source (i.e., the stagnation region), and the conversion from electromagnetic energy to plasma kinetic energy, which becomes effective beyond the light surface and/or FMS. A simple relation of the inflow energy $\hat{E}^{-}(\Psi)$ and the outflow energy $\hat{E}^{+}(\Psi)$ is assumed by matching the conditions of the ingoing and outgoing trans-fast magnetosonic flow solution. We find that a minimal outflow energy is required for the extraction of the rotational energy of a rotating black hole.

With flexible parameter choices, together with assumed electron heating, cooling, and distribution, our model is applicable for confronting theoretical GRMHD jet properties with observations at different scales, such as polarized jet emission (e.g., Broderick & McKinney 2010; Porth et al. 2011) and jet morphologies at large (e.g., Takahashi et al. 2018; Ogihara et al. 2019) and horizon (e.g., Broderick & Loeb 2009; Dexter et al. 2012; Chan et al. 2015; Mościbrodzka et al. 2016; Pu et al. 2017; Ryan et al. 2018; Chael et al. 2019; Event Horizon Telescope Collaboration et al. 2019e; Mościbrodzka & Falcke 2013) scales. With a prompt model construction for a given set of parameters, our model is also suitable for constraining preferred parameters in accreting black hole systems by systematically exploring the parameter space (e.g., Broderick et al. 2009, 2011, 2016).

We thank the anonymous referee for valuable comments. H.Y.P. is supported by the Perimeter Institute for Theoretical Physics. Research at the Perimeter Institute is supported in part by the Government of Canada through the Department of Innovation, Science and Economic Development Canada and by the Province of Ontario through the Ministry of Colleges and Universities. M.T. is supported by JSPS KAKENHI grant No. 17K05439 and DAIKO FOUNDATION. This research has made use of the NASA Astrophysics Data System.

Appendix A
Flowchart for the Semianalytical Model

A flowchart for the semianalytical approach described in Section 2 is summarized in Figure 12. By describing the black hole magnetosphere with black hole spin a, field configuration $\Psi(p)$, and magnetic field angular velocity $\Omega(\Psi)$, we can determine the stagnation surface $r_s(a, \Psi, \Omega_F)$, which separates the regions of the inflow (indicated by the superscript "−") and the outflow (indicated by the superscript "+"). We then use the specific flow energy of the outflow $\hat{E}^{+}(\Psi)$, a streamline conserved quantity, as the boundary condition of the GRMHD solution, with which the location of the Alfvén surface $r_{\rm A}^{+}(\Psi)$ and the angular momentum of the flow $\hat{L}^{+}(\Psi)$, another streamline conserved quantity, are simultaneously determined, and the Alfvén Mach number $M^{+}(r; \Psi)$ and poloidal velocity $u_p^{+}(r; \Psi)$ of the outflow can be algebraically solved by using Equation (11). Along each magnetic field line, the inflow solution is consistently solved by applying the matching condition for the flow energy $\hat{E}^{-}(\Psi)$ and pitch angle $\xi^{-}(r; \Psi)$. The relativistic jet powered by a rotating black hole should satisfy the following conditions: $0 < \Omega_F < \Omega_{\rm H}$ and $\hat{E}^{+} > 2$. Note that this procedure is for the case of a stationary solution, so it is also easy to reverse ($B \rightarrow A$).

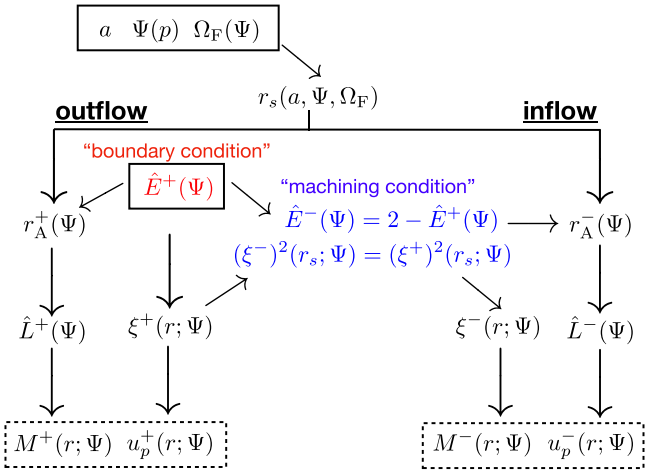

Figure 12. Overview of modeling Poynting flux-dominated trans-fast magnetosonic flow powered by a rotating black hole, as described in Section 2. The flow structure is semianalytically computed after assigning four parameters in the model: black hole spin a, magnetic field configuration Ψ, magnetic field angular velocity $\Omega_F(\Psi)$, and total energy of the outflow $\hat{E}^{+}(\Psi)$ across the magnetic field lines Ψ. The solid boxes indicate the input parameters, and the dashed boxes indicate the output GRMHD flow solution. The symbol $A \rightarrow B$ indicates that B can be computed from A. See Appendix A for details.

Appendix B
Flow Acceleration and Its Dependence on the Field Configuration

The relation of the efficiency of SRMHD flow acceleration and the magnetic field geometry has been extensively discussed in previous works. It is shown that for an infinite magnetically dominated plasma, the flow velocity is similar to the drift velocity (Narayan et al. 2007; Tchekhovskoy et al. 2008), and the Lorentz factor γ can be decomposed into (Tchekhovskoy et al. 2008, 2009; Komissarov et al. 2009)

$$\frac{1}{\gamma^2} = \frac{1}{\gamma_1^2} + \frac{1}{\gamma_2^2}, \tag{37}$$

where

$$\gamma_1^2 = \frac{B^2}{B_p^2}, \tag{38}$$

$$\gamma_2^2 = \frac{B^2}{B_\phi^2 - E_p^2}, \tag{39}$$

where E_p is the strength of the poloidal electric field and B_p and B_ϕ are the poloidal and toroidal components of the magnetic field B. Two types of acceleration regime exist: the first term in Equation (37) corresponds to a *linear* (faster) acceleration, and the second term in Equation (37), which is related to the field configuration and the poloidal radius of the curvature of the field lines, corresponds to a *logarithmic* (slower) acceleration. In the detailed analysis in Tchekhovskoy et al. (2008), it is shown that for a field configuration $\Psi \propto r^p(1 - \cos\theta)$, the second term is negligible, $p \geqslant 1$, and all of the electromagnetic energy will eventually convert to the kinetic energy of the flow. It is further pointed out in Tchekhovskoy et al. (2009) that, while the first term is always dominant close to the compact object, the second term becomes dominant beyond a "causality surface" introduced in Tchekhovskoy et al. (2009). While the FMS marks the boundary beyond which the flow can no longer

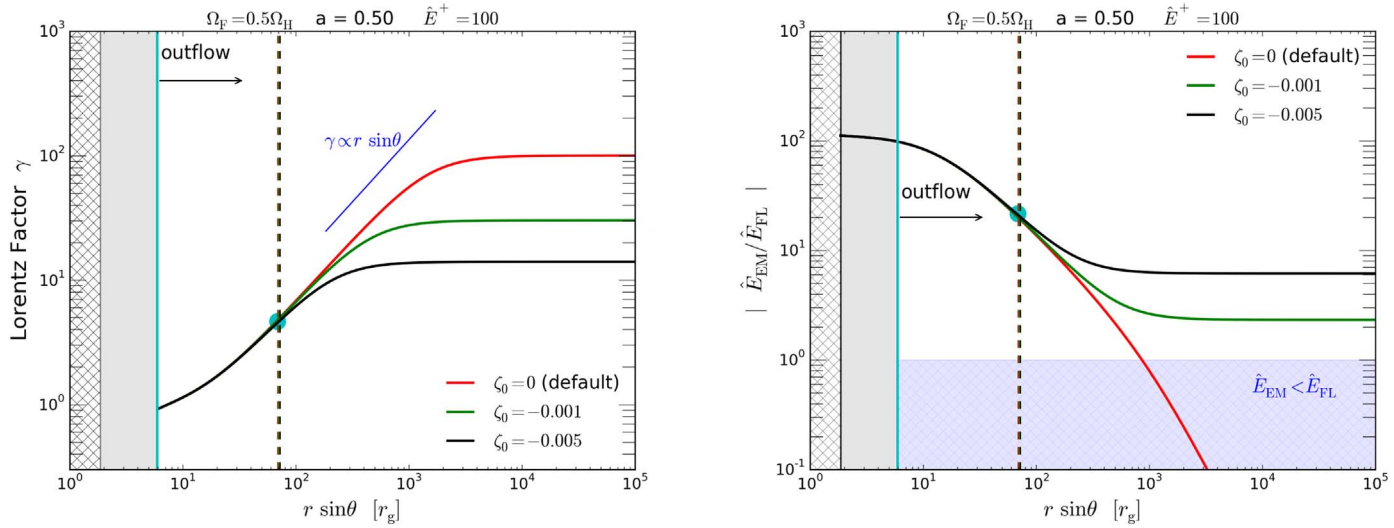

Figure 13. Outflow solutions of different choices of ζ_0, with the same setup as in Figures 3 and 4. The red profile shows the case $\zeta_0 = 0$, the default value in our model. Left panel: Lorentz factor γ of the flow. Right panel: the ratio between the electromagnetic energy and particle energy as a function of distance. The location of the FMS for each case is shown by the corresponding vertical dashed lines, which are almost overlapped with each other. The theoretical predicted value at the FMS from the perturbation method (Beskin & Nokhrina 2006) for an SRMHD flow is overlapped by the filled cyan circle. The choice of $\zeta_0 = 0$ ensures a linear acceleration and an efficient conversion from electromagnetic to kinetic energy. A slight deviation from $\zeta_0 = 0$ can further modify the conversion efficiency and the growth of the Lorentz factor, but only beyond the FMS.

communicate with its upstream *along* a streamline, the acceleration is also related to the communication *across* the streamlines. The causality surface is therefore defined as the area beyond which the jet can no longer communicate with the jet rotation axis. However, the causality surface is always located beyond the FMS. Therefore, including the consideration of the causality surface effect and the transition of the two different acceleration regime would only modify the acceleration properties beyond the FMS.

In our model, the acceleration properties are associated with the term ζ_0 in Equation (15). To demonstrate the effect of nonzero ζ_0, we compare the parabolic outflow solution for the case $\hat{E}^+ = 100$ shown in Figure 3 with different choices of ζ_0 in Figure 13. The right panel shows the energy conversion efficiency from electromagnetic part to the particle part. The vertical dashed lines (which are almost overlapped with each other) indicate the location of the FMSs for different choices of ζ_0. A choice of $\zeta_0 = 0$ actually guarantees the linear acceleration (the first term in Equation (37)), and therefore efficient energy conversion is obtained ($|\hat{E}^+_{EM}/\hat{E}^+_{FL}| < 1$) far beyond the outer FMS, while for $\zeta_0 < 0$, the flows remain magnetically dominated ($|\hat{E}^+_{EM}/\hat{E}^+_{FL}| > 1$). Note that for $\zeta_0 > 0$, the flow velocity (or the Alfvén Mach number) becomes infinitely large at a critical radius (see TT03). We therefore ignore the effect of the second term in Equation (37) and adopt $\zeta_0 = 0$ as the default value, which ensures that $\gamma \approx \gamma_1(\propto r\sin\theta)$ (Tchekhovskoy et al. 2008, 2009; Komissarov et al. 2009) can be properly realized (see Figures 3 and 5).

It is possible to include the transition from linear to logarithmic growth by further fine-tuning of ζ_0 with a generalized function $\zeta_0(\Psi) = \zeta_0(p, \hat{E}^+(\Psi), \eta(\Psi))$, depending on the location of the causality surface for a specific black hole magnetosphere. Nevertheless, as explained before, including the consideration of the causality surface effect and the transition of two different accelerations would only modify the acceleration properties beyond the FMS. This is shown by the fact that the flow solutions of different choice of ζ_0 are similar before passing the cyan circle. Thus, consideration of where the FMS will occur will be key in estimating the jet acceleration region.

ORCID iDs

Hung-Yi Pu https://orcid.org/0000-0001-9270-8812

References

Algaba, J. C., Nakamura, M., Asada, K., & Lee, S. S. 2017, ApJ, 834, 65
Asada, K., Nakamura, M., Doi, A., Nagai, H., & Inoue, M. 2014, ApJL, 781, L2
Beskin, V. S. (ed.) 2009, MHD Flows in Compact Astrophysical Objects: Accretion, Winds and Jets (Berlin: Springer)
Beskin, V. S., Kuznetsova, I. V., & Rafikov, R. R. 1998, MNRAS, 299, 341
Beskin, V. S., & Nokhrina, E. E. 2006, MNRAS, 367, 375
Blandford, R. D., & Payne, D. G. 1982, MNRAS, 199, 883
Blandford, R. D., & Znajek, R. L. 1977, MNRAS, 179, 433
Broderick, A. E., Fish, V. L., Doeleman, S. S., et al. 2009, ApJ, 697, 45
Broderick, A. E., Fish, V. L., Doeleman, S. S., et al. 2011, ApJ, 735, 110
Broderick, A. E., Fish, V. L., Johnson, M. D., et al. 2016, ApJ, 820, 137
Broderick, A. E., & Loeb, A. 2009, ApJ, 697, 1164
Broderick, A. E., & McKinney, J. C. 2010, ApJ, 725, 750
Broderick, A. E., & Tchekhovskoy, A. 2015, ApJ, 809, 97
Bruni, G., Gómez, J. L., Casadio, C., et al. 2017, A&A, 604, A111
Camenzind, M. 1986a, A&A, 156, 137
Camenzind, M. 1986b, A&A, 162, 32
Camenzind, M. 1987, A&A, 184, 341
Chael, A., Narayan, R., & Johnson, M. D. 2019, MNRAS, 486, 2873
Chan, C.-K., Psaltis, D., Özel, F., et al. 2015, ApJ, 812, 103
Chang, Z., Lin, H.-N., & Jiang, Y. 2012, ApJ, 759, 129
Chantry, L., Cayatte, V., Sauty, C., et al. 2018, A&A, 612, A63
Chatterjee, K., Liska, M., Tchekhovskoy, A., et al. 2019, MNRAS, 490, 2200
Contopoulos, I., Kazanas, D., & Fendt, C. 1999, ApJ, 511, 351
Contopoulos, J. 1995, ApJ, 446, 67
Dexter, J., McKinney, J. C., & Agol, E. 2012, MNRAS, 421, 1517
Event Horizon Telescope Collaboration, Akiyama, K., Alberdi, A., et al. 2019a, ApJL, 875, L1
Event Horizon Telescope Collaboration, Akiyama, K., Alberdi, A., et al. 2019b, ApJL, 875, L2
Event Horizon Telescope Collaboration, Akiyama, K., Alberdi, A., et al. 2019c, ApJL, 875, L3

Event Horizon Telescope Collaboration, Akiyama, K., Alberdi, A., et al. 2019d, ApJL, 875, L4
Event Horizon Telescope Collaboration, Akiyama, K., Alberdi, A., et al. 2019e, ApJL, 875, L5
Event Horizon Telescope Collaboration, Akiyama, K., Alberdi, A., et al. 2019f, ApJL, 875, L6
Fabian, A. C. 2012, ARA&A, 50, 455
Fender, R., Wu, K., Johnston, H., et al. 2004, Natur, 427, 222
Fendt, C. 1997, A&A, 319, 1025
Fendt, C., & Camenzind, M. 1996, A&A, 313, 591
Fendt, C., Camenzind, M., & Appl, S. 1995, A&A, 300, 791
Fendt, C., & Greiner, J. 2001, A&A, 369, 308
Globus, N., Sauty, C., Cayatte, V., et al. 2014, PhRvD, 89, 124015
Hada, K., Kino, M., Doi, A., et al. 2013, ApJ, 775, 70
Hada, K., Kino, M., Doi, A., et al. 2016, ApJ, 817, 131
Hawley, J. F., & Krolik, J. H. 2006, ApJ, 641, 103
Hirotani, K., & Pu, H.-Y. 2016, ApJ, 818, 50
Homan, D. C., Lister, M. L., Kovalev, Y. Y., et al. 2015, ApJ, 798, 134
Hovatta, T., Lister, M. L., Aller, M. F., et al. 2012, AJ, 144, 105
Huang, L., Pan, Z., & Yu, C. 2019, ApJ, 880, 93
Jeter, B., Broderick, A. E., & Gold, R. 2018, MNRAS, tmp, 636
Kino, M., Takahara, F., Hada, K., & Doi, A. 2014, ApJ, 786, 5
Koide, S. 2003, PhRvD, 67, 104010
Komissarov, S. S., Vlahakis, N., Königl, A., & Barkov, M. V. 2009, MNRAS, 394, 1182
Levinson, A., & Rieger, F. 2011, ApJ, 730, 123
Liska, M., Hesp, C., Tchekhovskoy, A., et al. 2018, MNRAS, 474, L81
Lyubarsky, Y. 2009, ApJ, 698, 1570
Lyubarsky, Y. E. 2010, MNRAS, 402, 353
McKinley, B., Tingay, S. J., Carretti, E., et al. 2018, MNRAS, 474, 4056
McKinney, J. C. 2006, MNRAS, 368, 1561
McKinney, J. C., & Gammie, C. F. 2004, ApJ, 611, 977
McKinney, J. C., & Narayan, R. 2007, MNRAS, 375, 531
Meliani, Z., Sauty, C., Vlahakis, N., et al. 2006, A&A, 447, 797
Michel, F. C. 1969, ApJ, 158, 727
Miller-Jones, J. C. A., Sivakoff, G. R., Altamirano, D., et al. 2012, MNRAS, 421, 468
Mościbrodzka, M., & Falcke, H. 2013, A&A, 559, L3
Mościbrodzka, M., Falcke, H., & Shiokawa, H. 2016, A&A, 586, A38
Mościbrodzka, M., Gammie, C. F., Dolence, J. C., et al. 2011, ApJ, 735, 9
Nakamura, M., Asada, K., Hada, K., et al. 2018, ApJ, 868, 146
Narayan, R., McKinney, J. C., & Farmer, A. J. 2007, MNRAS, 375, 548
Narayan, R., SÄdowski, A., Penna, R. F., et al. 2012, MNRAS, 426, 3241
Nathanail, A., & Contopoulos, I. 2014, ApJ, 788, 186
Nava, L., Desiante, R., Longo, F., et al. 2017, MNRAS, 465, 811
Nitta, S.-Y., Takahashi, M., & Tomimatsu, A. 1991, PhRvD, 44, 2295
Ogihara, T., Takahashi, K., & Toma, K. 2019, ApJ, 877, 19
O'Riordan, M., Pe'er, A., & McKinney, J. C. 2018, ApJ, 853, 44
Pan, Z., Yu, C., & Huang, L. 2017, ApJ, 836, 193
Phinney, E. S. 1983, PhD thesis, Univ. Cambridge
Polko, P., Meier, D. L., & Markoff, S. 2013, MNRAS, 428, 587
Polko, P., Meier, D. L., & Markoff, S. 2014, MNRAS, 438, 959
Porth, O., Fendt, C., Meliani, Z., & Vaidya, B. 2011, ApJ, 737, 42
Pu, H.-Y., Nakamura, M., Hirotani, K., et al. 2015, ApJ, 801, 56
Pu, H.-Y., Wu, K., Younsi, Z., et al. 2017, ApJ, 845, 160
Pushkarev, A. B., Kovalev, Y. Y., Lister, M. L., & Savolainen, T. 2017, MNRAS, 468, 4992
Rushton, A. P., Miller-Jones, J. C. A., Curran, P. A., et al. 2017, MNRAS, 468, 2788
Ryan, B. R., Ressler, S. M., Dolence, J. C., et al. 2018, ApJ, 864, 126
Ryde, F., Lundman, C., & Acuner, Z. 2017, MNRAS, 472, 1897
Sauty, C., & Tsinganos, K. 1994, A&A, 287, 893
Takahashi, K., Toma, K., Kino, M., Nakamura, M., & Hada, K. 2018, ApJ, 868, 82
Takahashi, M. 2002, ApJ, 570, 264
Takahashi, M., Nitta, S., Tatematsu, Y., & Tomimatsu, A 1990, ApJ, 363, 206
Takahashi, M., & Shibata, S. 1998, PASJ, 50, 271
Takahashi, M., & Tomimatsu, A. 2008, PhRvD, 78, 023012
Tchekhovskoy, A., McKinney, J. C., & Narayan, R. 2008, MNRAS, 388, 551
Tchekhovskoy, A., McKinney, J. C., & Narayan, R. 2009, ApJ, 699, 1789
Tchekhovskoy, A., Narayan, R., & McKinney, J. C. 2010, ApJ, 711, 50
Tomimatsu, A., Matsuoka, T., & Takahashi, M. 2001, PhRvD, 64, 123003
Tomimatsu, A., & Takahashi, M. 2003, ApJ, 592, 321
Tsinganos, K. 2010, MSAIS, 15, 102
Vlahakis, N. 2004, ApJ, 600, 324
Vlahakis, N., Tsinganos, K., Sauty, C., et al. 2000, MNRAS, 318, 417